Unsteadiness in condensing flow: dynamics of internal flows with phase transition and application to turbomachinery

G H Schnerr

Fachgebiet Gasdynamik, Lehrstuhl fur Fluidmechanik, Technische Universität München, Boltzmannstraße 15, D-85748 Garching, Germany

Abstract: Steady flows of condensable fluids may become unsteady if one component of the fluid starts to condense. In high-speed expansion flows, typical for large-scale steam turbines, the subcooled vapour state collapses after nucleation, typically in flow regimes close to Mach number 1. After the formation of steady shocks, instantaneous thermal choking initiates self-excited high-frequency oscillations which is the focus of this article. The driving mechanism is the interaction of compressibility and energy supply in flows close to maximum mass flux density and is therefore not controlled by the viscosity of the fluid. Additional viscosity-driven excitation mechanisms exist and superpose the primary diabatic instability, especially in axial cascades. Typical are shedded shear layers from blade trailing edges and the periodic interference of wakes separating from the stator with the rotor blades. This article presents a review of the authors and various co-workers' research, supplemented by important references to complete the subject under consideration. This article starts with an introduction in the most simple flow model of given heat addition in constant area flow and ends with mixed homogeneous/heterogeneous condensation in a transonic axial cascade stage with a high-resolution sliding interface for preservation of submicron condensate convected from the stator into the rotor. Numerical simulations are compared with experiments of flows with and without carrier gas.

Keywords: transonic two-phase flow, thermal choking, instability, moving shocks, self-excited oscillations

1 INTRODUCTION

Partial phase transitions in rapid expansions of mixtures of pure vapours and of vapour/carrier gas prevail in many engineering applications. Together with transonic aerodynamics, the steam turbine is certainly an important representative of these flows. Because the last stages of low-pressure (LP) steam turbines are directly connected with the condenser having necessarily low values of pressure and temperature, the working fluid starts already to condense flowing through the last blade passages. The scaling of the rotor of the last stage with a diameter of 3–4 m, together with the line frequency of 50 Hz (Europe) or 60 Hz (USA), makes clear that the maximum circumferential speed is of the order of 600 m/s. Therefore, the blade-to-blade flow in rotors experiences strong compressibility effects. Starting at the inlet, the flow accelerates typically from $M_1 = 0.4$ to supersonic flow at the outlet with $M_2 = 1.2-1.4$. Within a few microseconds, the temperature of the vapour decreases below the equilibrium saturation limit. This is because the phase change proceeds at a finite rate and there is no sufficient time for equilibrium condensation to occur.

As a first approach, the relative flow through an axial rotor can be regarded as an expansion flow through a Laval nozzle, with low pressure and supersonic Mach number at the exit and with non-equilibrium condensation of the working fluid inside. Further extension of this model by inclusion of the rotor/stator interaction requires introduction of non-uniform flow conditions at the inlet of this nozzle model. Finally, blade wake separation from

the trailing edge initiates periodic disturbances at the outlet. However, these unsteady excitation mechanisms already exist in single-phase flow and are superimposed by unsteady boundary layer separation owing to shock/boundary layer interaction on the blade surface. In case of condensation, it is necessary to understand how the liquid phase forms in non-equilibrium and how it interacts with single-phase flow dynamics.

It is obvious that coincidence of strong mechanisms, such as the latent heat from condensation is added to the flow close to Mach number 1, i.e. at maximum mass flux density $\rho w = \rho^* w^*$, and the well-known equivalence of energy and mass supply in compressible flow, always produces intense interactions with substantial changes of the flow pattern, for instance, by formation of additional shocks or high-frequency oscillations.

To describe the physics of the non-linear problem and to make the resulting flow dynamics easily understandable, this article starts with an introduction of compressible flows in fluid dynamics with given heat addition $Q = \text{const.}$ and the simplest case of constant cross-sectional area, $A = \text{const.}$ The great advantage of this model is that the conservation laws reduce to algebraic equations and their solutions reveal important phenomena exploring details of much more complex multi-dimensional flows, e.g. it can be recognized immediately why under certain conditions steadiness does not exist and why unsteady flow must occur. This article considers the phenomenon of thermal choking in more detail by extending to flows with given heat source distribution $Q(x)$ inside a given area distribution $A(x)$. It shows how the flow avoids choking by forming additional steady shocks. In conclusion, a given heat source distribution $Q(x)$ i.e. heat addition, without two-way coupling with the flow and without inclusion of the kinetics of the phase transition itself, re-establishes a new flow topology which makes the specified added heat consistent with all existing steady flow conditions, with or without supplementary steady shocks and to remain in steady state.

To proceed to a more complete model with latent heat addition from partial condensation of the working fluid, models for the formation of the liquid phase must be added and the reaction of compression waves and shocks on the phase transition process itself must be considered. This leads to conditions where steady shocks are no more possible and explains the formation of cyclic self-excited instabilities with moving shocks. At present, it is known that how, after bifurcations, higher-order instabilities develop with instantaneous change of the flow pattern and combined by doubling of the oscillation frequency.

As this mechanism depends on interactions of compressibility and energy supply, it is not dominated by viscosity effects. Additional unsteady excitation mechanisms play a role and have to be considered if boundary layers or blade wake separation are coupled with the primary inviscid flow instability.

2 COMPRESSIBLE FLOWS WITH GIVEN INTERNAL HEAT ADDITION

2.1 Heat addition Q = const. in constant area flow, A = const.

2.1.1 Governing equations

For steady, constant-area flow of an inviscid perfect gas/vapour and neglecting heat conduction, the governing equations of the conservation of mass, momentum, and energy can be written in integrated form

$$\rho_1 w_1 = \rho_2 w_2 \tag{1}$$

$$p_1 + \rho_1 w_1^2 = p_2 + \rho_2 w_2^2 \tag{2}$$

$$\left(c_p T_1 + \frac{w_1^2}{2}\right)(1 + Q) = c_p T_2 + \frac{w_2^2}{2} \tag{3}$$

with the equation of state

$$p = \rho R T \tag{4}$$

and the normalized amount of the heat source

$$Q = \frac{q}{c_p T_1 + (w_1^2/2)} = \frac{q}{c_p T_{01}} \begin{cases} >0 \text{ heat addition} \\ <0 \text{ heat removal} \end{cases} \tag{5}$$

The subscripts 1 and 2 refer to the static values of the flow properties ahead and behind the area of heat addition, respectively, and the subscripts 01 and 02 represent the corresponding stagnation values (Fig. 1). This is the most simplified example of a flow with heat addition without any length- or time-scale. The non-linear system of algebraic equations (1) to (4) yields several solutions depending on whether the initial flow is supersonic or
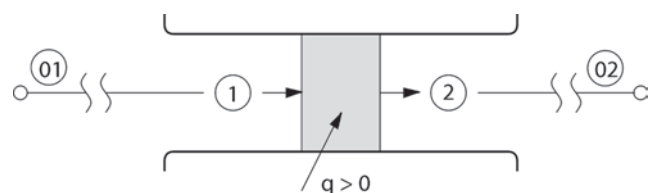

Fig. 1 Heat addition in constant area flow, A = const.; shaded area: zone of heat addition

subsonic and on the boundary conditions at the exit of the tube, e.g. on the static pressure p_e. For the nature of the condensation problem with always slightly supersonic onset Mach numbers, it is restricted to $M_1 > 1$.

2.1.2 Static properties after supersonic heat addition

Systematic elimination yields the following system for the unknowns behind the heat addition [1, 2]

$$\left(\frac{w_2}{w_1}\right)_{1,2} = 1 - \frac{1}{\gamma+1}\frac{M_1^2-1}{M_1^2}\left[1 \mp \sqrt{1 - \frac{Q}{Q_{max}}}\right] \quad (6)$$

$$\left(\frac{\rho_1}{\rho_2}\right)_{1,2} = 1 - \frac{1}{\gamma+1}\frac{M_1^2-1}{M_1^2}\left[1 \mp \sqrt{1 - \frac{Q}{Q_{max}}}\right] \quad (7)$$

$$\left(\frac{p_2}{p_1}\right)_{1,2} = 1 + \frac{\gamma}{\gamma+1}(M_1^2-1)\left[1 \mp \sqrt{1 - \frac{Q}{Q_{max}}}\right] \quad (8)$$

$$\left(\frac{T_2}{T_1}\right)_{1,2} = \left(1 + \frac{\gamma}{\gamma+1}(M_1^2-1)\right)\left[1 \mp \sqrt{1 - \frac{Q}{Q_{max}}}\right]$$
$$\times \left(1 - \frac{1}{\gamma+1}\frac{M_1^2-1}{M_1^2}\right)\left[1 \mp \sqrt{1 - \frac{Q}{Q_{max}}}\right] \quad (9)$$

$$(M_2^2)_{1,2} = M_1^2 \frac{1 - (1/(\gamma+1))((M_1^2-1)/M_1^2)}{1 + (\gamma/(\gamma+1))(M_1^2-1)} \frac{\times[1 \mp \sqrt{1-(Q/Q_{max})}]}{\times[1 \mp \sqrt{1-(Q/Q_{max})}]} \quad (10)$$

With $Q = 0$ and $M_1 > 1$, these results reduce to the identity and the adiabatic normal shock solution. Therefore, the effect of heat addition can be understood as a disturbance of these basic solutions. The upper sign in front of the square root corresponds to the so-called weak solution, the lower sign to the shock solution. It is clear that the temperature ratio $(T_2/T_1)_{1,2}$ can also be calculated by inserting the density ratio $(\rho_1/\rho_2)_{1,2}$ (equation (7)) and the static pressure ratio $(p_2/p_1)_{1,2}$ (equation (8)) into the ideal gas equation.

Both solutions (1) and (2) behind heat addition are connected by a normal shock corresponding to the well-known Prandtl relationship

$$(w_2)_1(w_2)_2 = c_2^{*2}$$
$$(M_2^*)_1(M_2^*)_2 = 1 \quad (11)$$

For the condensation problem, it is important that for any given initial Mach number M_1, there exists an

upper limit of Q_{max} that exactly leads to $M_2 = 1$

$$Q_{max} = \frac{q_{max}}{c_p T_{01}} = \frac{(M_1^2-1)^2}{2(\gamma+1)M_1^2(1+((\gamma-1)/2)M_1^2)} \quad (12)$$

When heat addition leads to sonic conditions behind the supply, the flow is called thermally choked. For values $Q > Q_{max}$, the square roots yield imaginary values that means no steady-state solution exists. For heat removal $Q < 0$, no such limit exists. For $M_1 \to \infty$, Q approaches asymptotically a finite upper limit Q_{max} depending on the specific heat ratio γ (Fig. 2).

Preserving the threshold value of Q_{max} in transonic flow restricts the possible supply to small disturbances. For $M_1 \to 1$, Q_{max} vanishes to zero. Therefore, sonic flow in a constant area with $Q > 0$ must become unsteady. For water vapour and water vapour/carrier gas mixtures of $q/c_p T_{01} = 0.1$, condensation onset Mach numbers typically are below 1.3. From Fig. 3, it is evident that this is too high to remain in steady state and explains the necessary formation of unsteady phenomena.

The following graph shows various solutions for $M_1 > 1$ with heat addition and heat removal. Figure 4 shows that heat addition shifts the resulting Mach number M_2 towards the critical state $M_2 = 1$ for both, the weak and the shock solutions. Compared with adiabatic flow, the static pressure increases and decreases for the weak and the shock solutions, respectively. The opposite tendency exists for a shock in condensing vapour with dispersed saturated droplets where the temperature
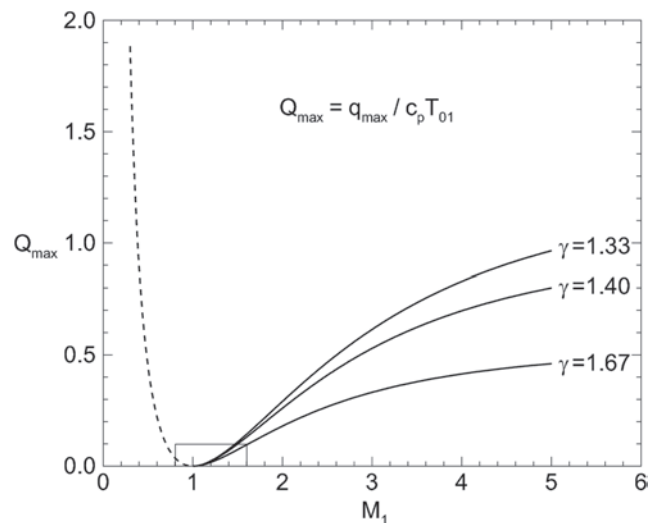
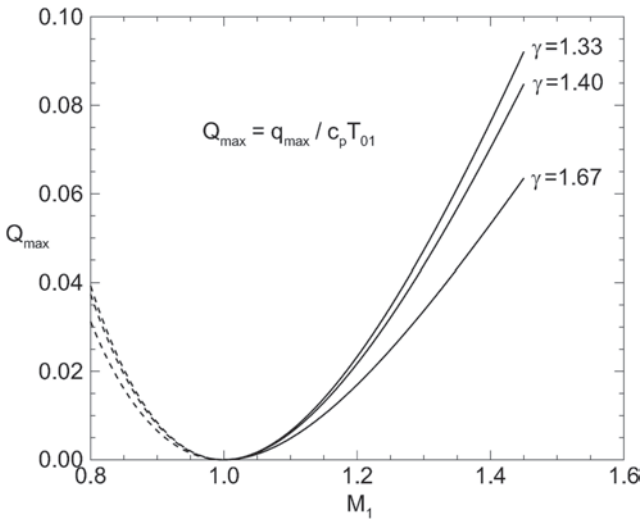**Fig. 2** Maximum heat addition Q_{max} in steady constant area flow depending on Mach number M_1 and specific heat ratio γ

Fig. 3 Transonic regime of maximum heat addition Q_{max} in steady constant area flow depending on Mach number M_1 and specific heat ratio γ

increase through the shock causes evaporation of droplets. This shock-induced evaporation happens typically at the rear boundary of clouds around airplanes flying at high angle of attack and/or with transonic Mach numbers at low altitudes with substantial natural humidity content in the atmosphere.

Figure 5 shows the Hugoniot curves for $Q = q/c_p T_{01} > 0$, $Q < 0$, and for adiabatic flow. The

Hugoniot curves for heat addition and removal are above and below the adiabatic curve, respectively [1, 2]

$$\frac{p_2}{p_1} = \frac{\gamma - 1}{\gamma + 1}$$
$$\times \frac{(2\gamma/(\gamma-1))\,(q/c_p T_1) + (\gamma+1)/(\gamma-1) - (\rho_1/\rho_2)}{\rho_1/\rho_2 - ((\gamma-1)/(\gamma+1))}$$

(13)

The intersection with the Rayleigh line

$$\frac{p_2}{p_1} - 1 = -\gamma M_1^2 \left(\frac{\rho_1}{\rho_2} - 1 \right)$$

(14)

yields all possible solutions. As quantitative example for $M_1 = 1.3$ and $Q_4 = 0.04$, M_2, p_2/p_1, ρ_2/ρ_1, and T_2/T_1 behind the heat addition are shown in Figs 6 and 7 for the weak and shock solutions, respectively.

What is different for heat addition in subsonic flow $M_1 < 1$? The previous discussion presumes that the initial conditions are known and kept constant. Because of the upstream influence of all disturbances in subsonic flow, an initial Mach number $M_1 < 1$ ahead of a heating zone immediately changes according to the boundary condition behind the heat addition and the strength of the upstream effect. Figure 8 shows a simplified model and demonstrates that for the constant pressure p_e at the subsonic exit the static pressure of the oncoming flow p_1 depends on the amount of heat addition itself. Because of the
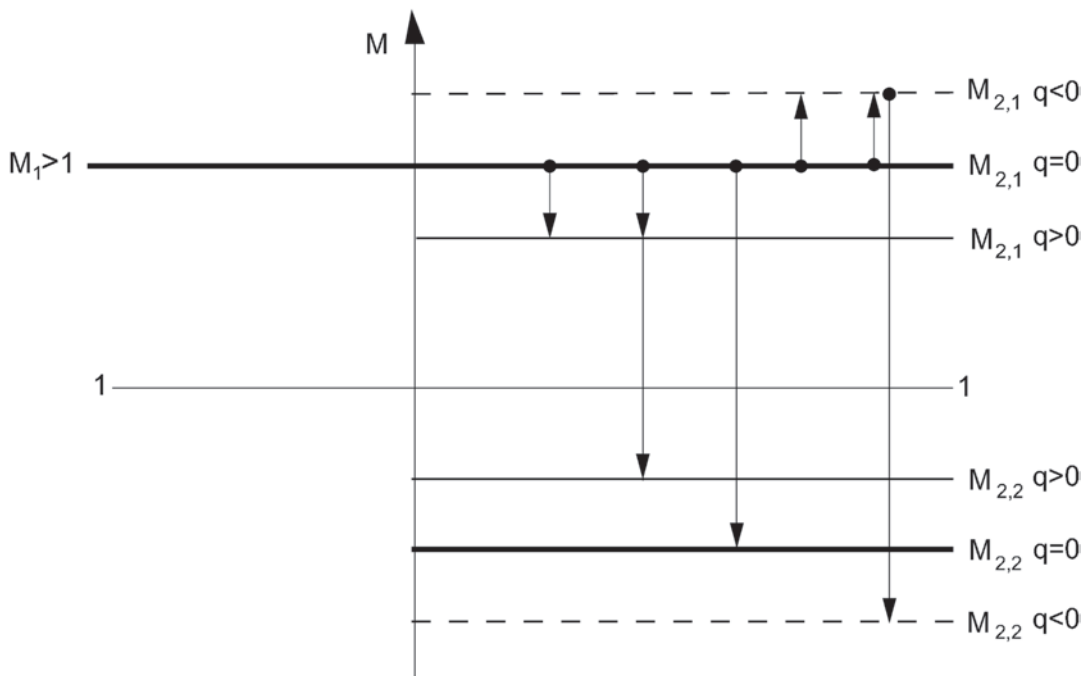

Fig. 4 Mach number M_2 in adiabatic flow ($q = 0$), with heat addition ($q > 0$), and with heat removal ($q < 0$); $M_{2,1}$ – weak solution; $M_{2,2}$ – shock solution
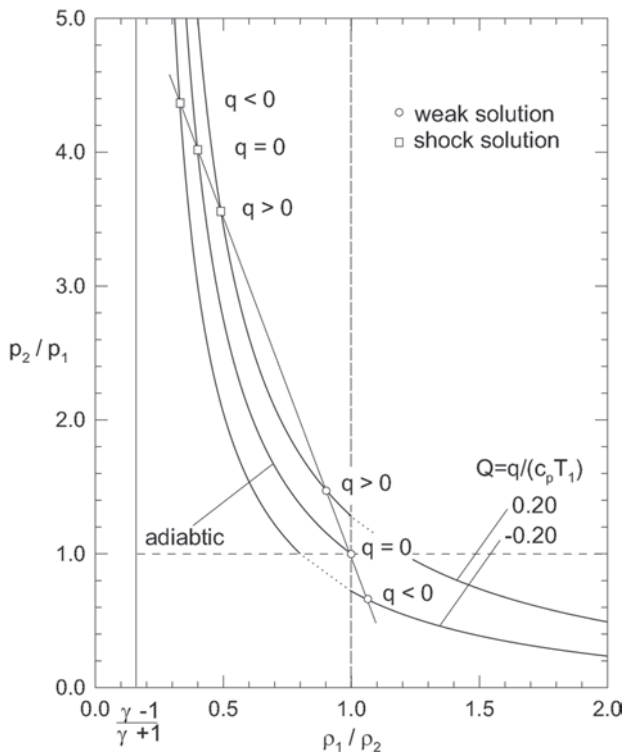
Fig. 5 Hugoniot curves for adiabatic flow, heat addition ($q > 0$), heat removal ($q < 0$), and Rayleigh line; solutions for $M_1 > 1$

second law of thermodynamics, shocks cannot exist in subsonic flow, although the entropy variation depending on the Mach number includes a mathematical solution in this region (Fig. 9). Therefore, in flows with subsonic heat addition, only weak solutions exist. Nevertheless, in tendency all trends of the results derived for supersonic heat addition (weak solution only) are inverted. The elliptical nature of the problem requires an iterative technique to find steady-state solutions for heat addition in subsonic flow.

2.1.3 Stagnation properties after supersonic heat addition

The increase of the stagnation temperature follows immediately from the energy conservation of equation (3)

$$
\left(c_p T_1 + \frac{w_1^2}{2}\right)(1 + Q) = c_p T_2 + \frac{w_2^2}{2} \quad \text{with } w_1 = w_2 = 0
$$
$$
c_p T_{01}(1 + Q) = c_p T_{02}
$$
$$
\frac{T_{02}}{T_{01}} = 1 + Q
$$

(15)

This result is independent of the Mach number and therefore valid for supersonic and subsonic

flows (Fig. 10(a)). Furthermore, it is valid for the weak and shock solutions because the stagnation temperature does not change across a steady adiabatic shock. The pressure ratio $(p_{02}/p_{01})_{1,2}$ is calculated by combining the standard isentropic relations for p_1/p_{01}, p_2/p_{02} with p_1/p_2 and equation (10) for M_2 giving

$$
\left(\frac{p_{02}}{p_{01}}\right)_{1,2} = \frac{\begin{aligned}&\{1 + (\gamma/(\gamma+1))(M_1^2 - 1)[\ ]\}\\ &\times\{1 + ((\gamma-1)/2)M_1^2(1 - (1/(\gamma+1))\\ &\times((M_1^2 - 1)/M_1^2)[\ ])/(1+\\ &(\gamma/(\gamma+1))(M_1^2 - 1)[\ ])\}^{\gamma/(\gamma-1)}\end{aligned}}{(1 + ((\gamma-1)/2)M_1^2)^{\gamma/(\gamma-1)}}
$$

(16)

with

$$
[\ ] = \left[1 \mp \sqrt{1 - \frac{Q}{Q_{max}}}\right]
$$

(17)

From the second law of thermodynamics, it follows immediately that the stagnation pressure ratio decreases by heat addition. For $M_1 \to \infty$ and $Q = Q_{max}$, i.e. $[\ ] = 1$, we obtain

$$
\lim_{\substack{M_1 \to \infty \\ Q = Q_{max}}}\left\{\left(\frac{p_{02}}{p_{01}}\right)_{1,2}\right\}
$$
$$
\sim \lim_{M_1 \to \infty} \frac{M_1^2\{M_1^2(1 - 1/(\gamma+1))\}^{\gamma/(\gamma-1)}}{M_1^{2(\gamma/(\gamma-1))}M_1^{2(\gamma/(\gamma-1))}}
$$
$$
\sim \lim_{M_1 \to \infty} \frac{1}{M_1^{2/(\gamma-1)}} = 0
$$

Figures 10(b) and (c) show the quantitative parameter range of the weak and shock solutions relevant for homogeneously condensing flows. The limiting curve $Q = Q_{max}$ corresponds to the solution of equation (12) describing the maximum amount of heat addition in steady flow and for given supersonic Mach number M_1 (Fig. 3). From Fig. 10(c) it follows that for the example under consideration with $M_1 = 1.3$ and $Q = q/c_p T_{01} = 0.04$, the entire stagnation pressure loss $(p_{02}/p_{01})_2$ is approximately 4 per cent. As the diabatic compression due to the supersonic heat addition shifts the supersonic Mach number close to the limiting curve $Q = Q_{max}$ with $M_2 = 1$, the remaining adiabatic shock is very weak and the stagnation pressure loss of this additional shock is therefore negligible. In this case, the entire stagnation pressure loss is completely controlled by the contribution of the heat addition $(\Delta p_0/p_{01})_q$. For comparison, an adiabatic normal shock starting at $M_1 = 1.3$ causes only about
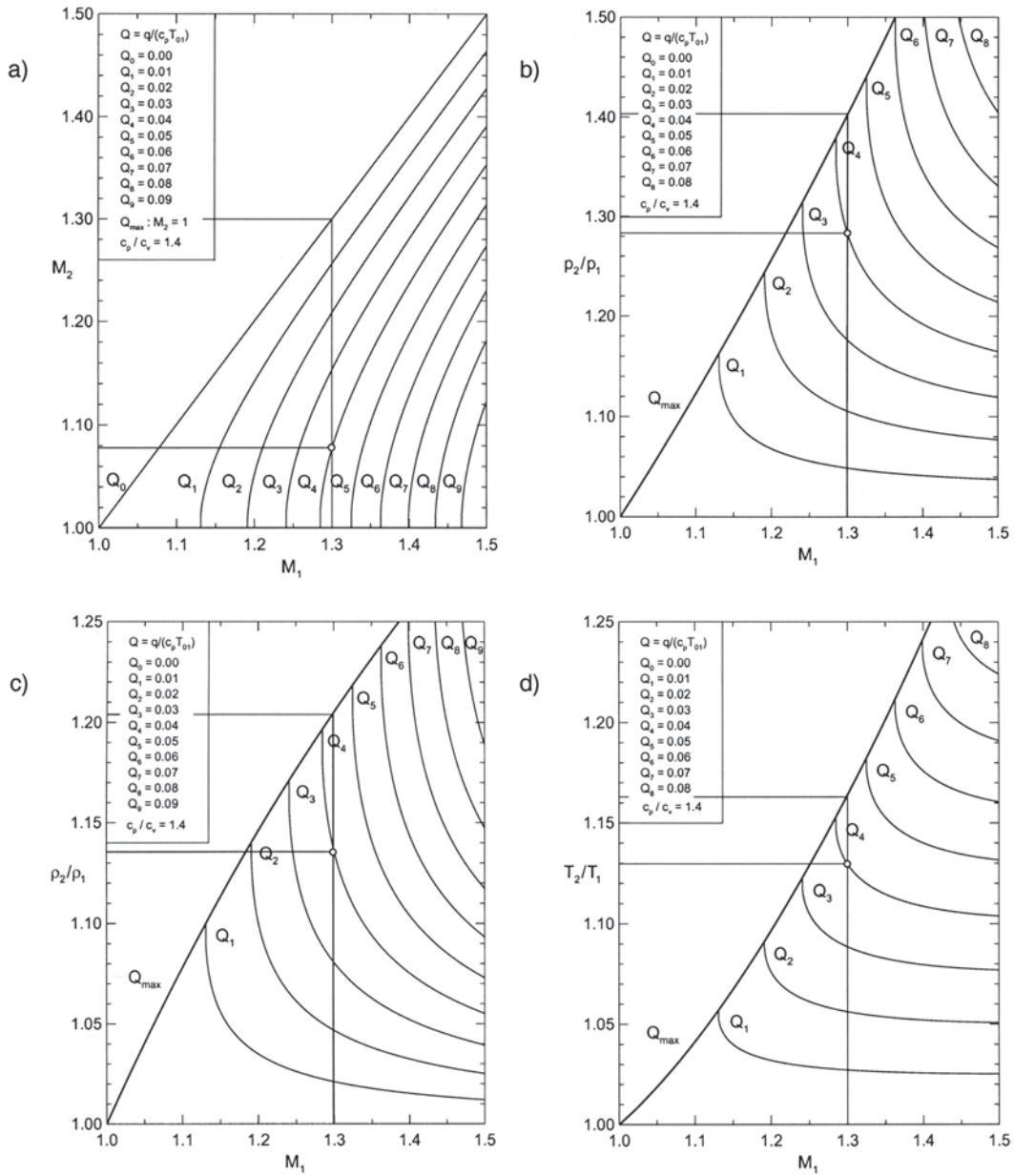
Fig. 6 Static properties after supersonic heat addition depending on M_1 – weak solution: (a) Mach number M_2; (b) pressure ratio p_2/p_1; (c) density ratio ρ_2/ρ_1; (d) temperature ratio T_2/T_1; the circle indicates the example with $M_1 = 1.3$ and $Q_4 = 0.04$

2 per cent stagnation pressure loss. For the stagnation density ratio (Fig. 10(d))

$$
\left(\frac{\rho_{02}}{\rho_{01}}\right)_{1,2} = \frac{\begin{array}{c}(1 + ((\gamma - 1)/2)M_1^2 \\ \times ((1 - (1/(\gamma + 1))((M_1^2 - 1)/M_1^2)[\ ])/(1 \\ + ((\gamma/(\gamma + 1))(M_1^2 - 1)[\ ]))^{1/(\gamma - 1)}\end{array}}{\begin{array}{c}(1 + ((\gamma - 1)/2)M_1^2)^{1/(\gamma - 1)} \\ \times (1 - (1/(\gamma + 1))((M_1^2 - 1)/M_1^2)[\ ])\end{array}}
$$

(18)

From the equation of state for a perfect gas law it follows that for heat addition, i.e. increase of T_0, the decrease of the stagnation pressure p_0 must be lower than the decrease of the stagnation density ρ_0.

2.1.4 Equivalence of heat and mass addition

If mass and heat are added to the flow, the conservation of mass changes into

$$
\rho_1 w_1 (1 + m) = \rho_2 w_2
$$

(19)

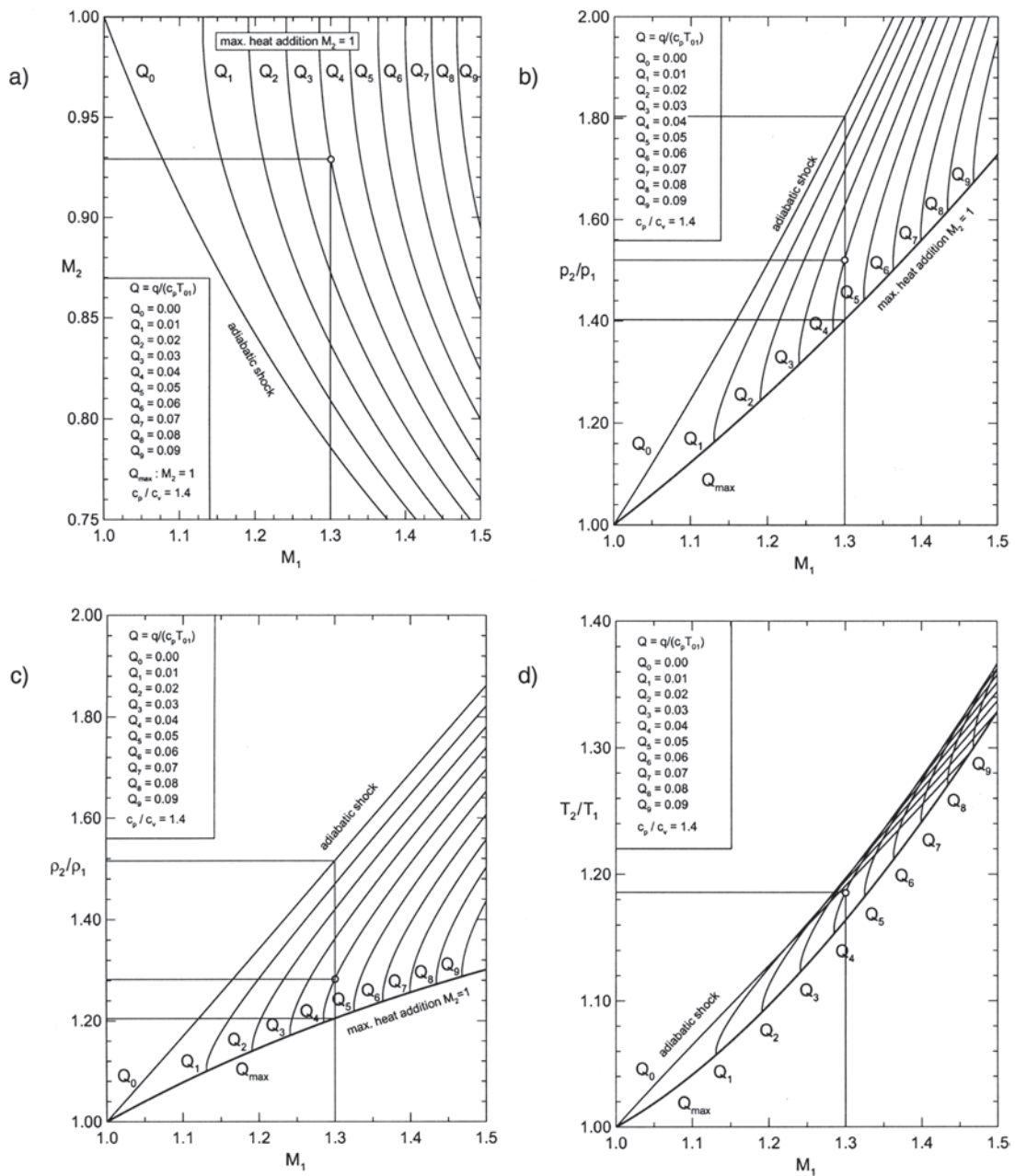whereas equations (2) to (5) of the system of governing equations remain unchanged. Here m is the

Fig. 7 Static properties after supersonic heat addition depending on M_1 – shock solution: (a) Mach number M_2; (b) pressure ratio p_2/p_1; (c) density ratio ρ_2/ρ_1; (d) temperature ratio T_2/T_1; the square indicates the example with $M_1 = 1.3$ and $Q_4 = 0.04$

normalized amount of mass addition

$$m = \frac{\varepsilon}{\rho_1 w_1} \qquad (20)$$

As before in case of energy supply (equation (3)), the present model assumes that mass is added to the flow by a mass source without any change of the momentum and energy conservation. Solving this new system of equation (19), equations (2) to (5) yield [1, 2]

$$\left(\frac{w_2}{w_1}\right)_{1,2}(1+m) = \left(\frac{\rho_1}{\rho_2}\right)_{1,2}(1+m)^2$$

$$= \frac{1}{\gamma+1}\left\{\gamma + \frac{1}{M_1^2}\right.$$

$$\pm \sqrt{\begin{array}{c} \left(\gamma + \dfrac{1}{M_1^2}\right)^2 - 2(\gamma+1) \\ \times (\dfrac{1}{M_1^2} + \dfrac{\gamma-1}{2})(1+Q)(1+m)^2 \end{array}}\left.\right\}$$
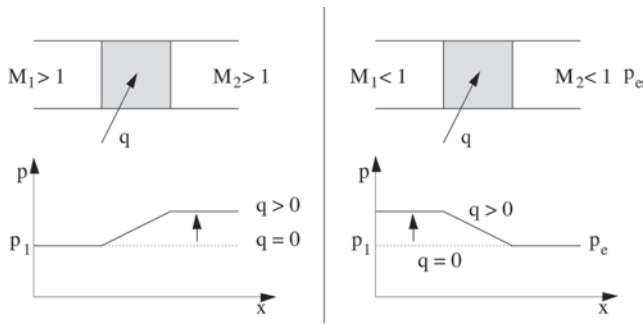
$$\qquad (21)$$

Fig. 8   Supersonic heat addition without upstream effect (left); subsonic heat addition with upstream effect for given static pressure p_e at the exit of the tube (right)

$$\left(\frac{p_2}{p_1}\right)_{1,2} = \frac{M_1^2}{\gamma+1}\left\{\gamma+\frac{1}{M_1^2}\right.$$

$$\left.\mp\gamma\sqrt{\begin{array}{c}\left(\gamma+\dfrac{1}{M_1^2}\right)^2-2(\gamma+1)\\[6pt]\times\left(\dfrac{1}{M_1^2}+\dfrac{\gamma-1}{2}\right)(1+Q)(1+m)^2\end{array}}\right\}$$

$$(22)$$

$$(M_2)_{1,2}^2 = \frac{\gamma+(1/M_1^2)\pm\sqrt{\begin{array}{c}(\gamma+(1/M_1^2))^2\\-2(\gamma+1)\\\times(1/M_1^2+(\gamma-1)/2)\\\times(1+Q)(1+m)^2\end{array}}}{\gamma+(1/M_1^2)\mp\gamma\sqrt{\begin{array}{c}(\gamma+(1/M_1^2))^2\\-2(\gamma+1)\\\times(1/M_1^2+(\gamma-1)/2)\\\times(1+Q)(1+m)^2\end{array}}}$$

$$(23)$$

From equations (21) to (23) it follows immediately that in the radicand the two factors $(1+Q)$ and $(1+m)^2$ are equivalent and can be exchanged by each other. This leads to the important conclusion that heat and mass additions in compressible flow are equivalent and emphasize again the tendency
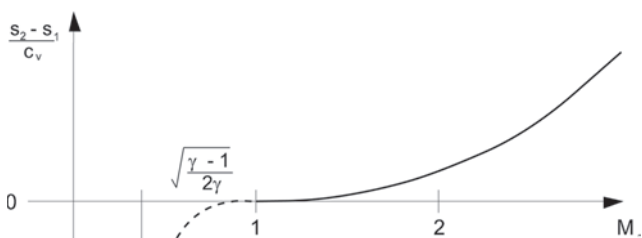

Fig. 9   Variation of specific entropy depending on M_1 across a normal adiabatic shock

of heat addition in compressible flows leading to thermal choking independent of whether the initial state is sub- or supersonic.

2.1.5   Unsteady state, $Q > Q_{max}$

If the amount of heat added to the flow exceeds Q_{max} for a given Mach number M_1, equations (6) to (10) yield complex results, i.e. no steady flow exists. This problem has been investigated by Bartlmä [3, 4] for different initial conditions. This article discusses the most interesting example when heat is added to a flow with $M_1 = 1$, i.e. when the flow ahead of the heat or equivalent mass addition is already under the condition of maximum mass flux density with $Q_{max} = 0$. The solution of this problem is instructive and shows the following interesting details (Fig. 11).

For $t < 0$, the steady flow is undisturbed with $M_1 = 1$ throughout in the tube. At $t = 0$ instantaneously a small amount of heat q' is added to the flow. Because of the incompatibility of any additional displacement effect caused by the equivalent mass addition, two shock waves (S_I and S_{II}) start instantaneously in front and behind the zone of heat addition and move monotonically upstream into the oncoming flow and downstream toward the exit of the tube, respectively. Owing to these two unsteady shock waves, the conditions ahead and behind the heat addition zone are altered in such a manner that the given amount of heat q' becomes consistent with steady flow across the heating zone. In other words, the variation of all variables, such as pressure, density, velocity, and Mach number across the heating zone, complies with the steady-state equations. Nevertheless, the whole problem is unsteady due to the monotonically moving shock waves in the far-field.

Figure 11 depicts the qualitative Mach number distribution and quantitative results for $q'/c_p T_1 = 0.1$ and the specific heat ratio $\gamma = 1.4$. Across the shock S_I, the Mach number decreases from $M_1 = 1$ to $M_5 = 0.654$ and, as expected for subsonic heat addition, it increases to $M_4 = 0.970$ but remains subsonic in region (4) behind the supply. Areas (3) and (4) are separated by the so-called contact surface C. It separates the heated fluid of region (4) and the colder fluid of region (3), which is compressed by the shock S_{II}. Owing to the acceleration of the flow across the moving shock S_{II} that moves into sonic flow with $M_2 = 1$, the Mach number behind S_{II} becomes slightly supersonic with $M_3 = 1.020$. Because of the condition of constant flow velocity across the contact surface and the higher temperature, i.e. higher speed of sound, in region (4) the Mach number changes from sub- to supersonic across the contact surface C. Figure 12 shows subsequently the static values of the
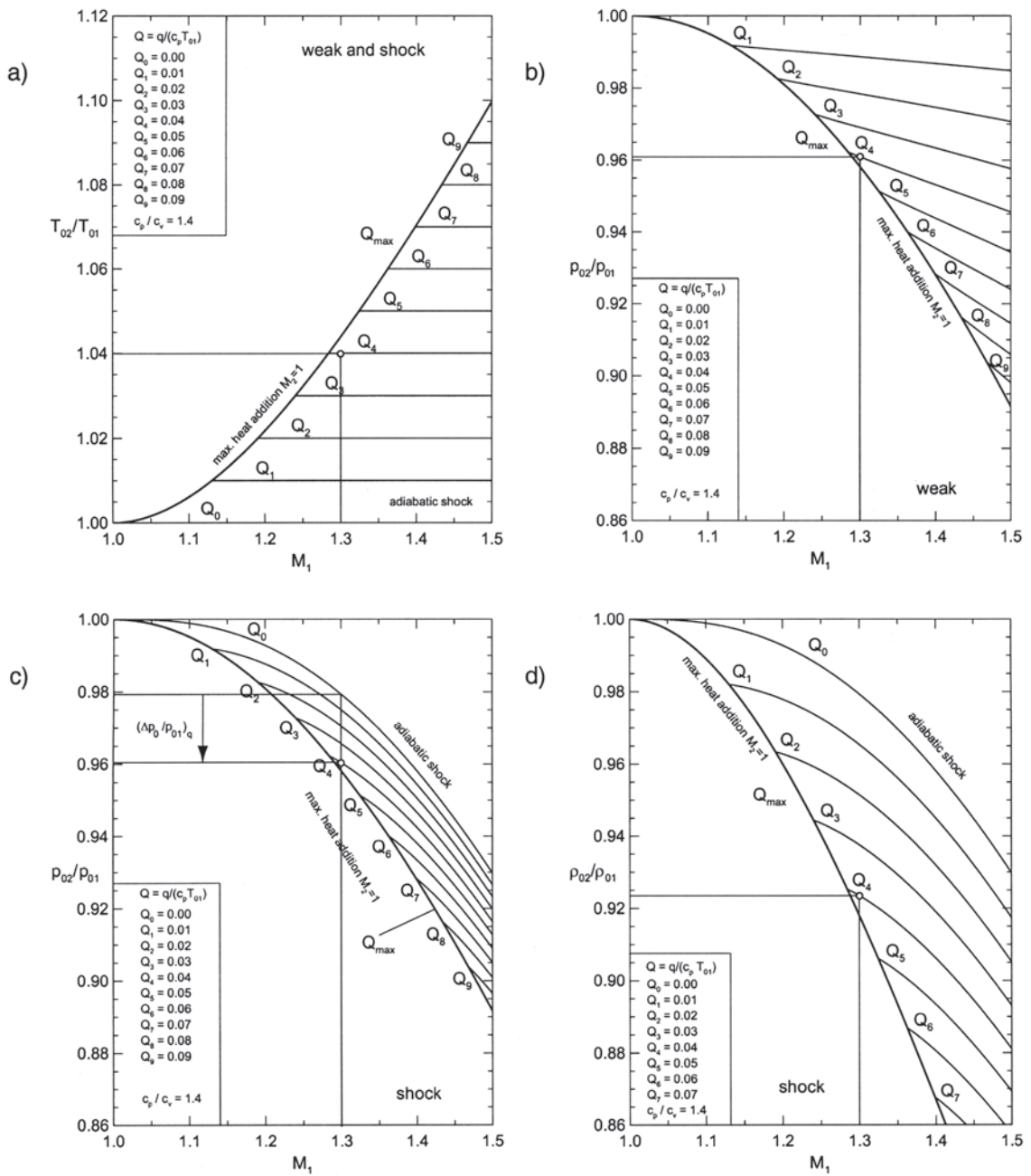
Fig. 10 Stagnation properties after supersonic heat addition depending on M_1; (a) temperature ratio T_{02}/T_{01} (weak and shock solutions): (b) pressure ratio p_{02}/p_{01} (weak solution); (c) pressure ratio p_{02}/p_{01} (shock solution); (d) density ratio ρ_{02}/ρ_{01} (shock solution); circles and squares correspond to the example with $M_1 = 1.3$ and $Q_4 = 0.04$

pressure ratio p/p_1, the density ratio ρ/ρ_1, and the temperature disturbance T/T_1.

2.2 Heat addition $Q(x)$ in one-dimensional nozzle flow, $A = A(x)$

2.2.1 Differential equations

For one-dimensional Laval nozzle flow (Fig. 13) with given heat addition, the system of governing equations reads for

mass:
$$\frac{1}{\rho}\frac{d\rho}{dx} + \frac{1}{w}\frac{dw}{dx} + \frac{1}{A}\frac{dA}{dx} = 0 \qquad (24)$$

momentum:
$$w\frac{dw}{dx} = -\frac{1}{\rho}\frac{dp}{dx} \qquad (25)$$

with $\gamma p/\rho = c^2$

$$\frac{1}{w}\frac{dw}{dx} + \frac{1}{\gamma M^2}\frac{1}{p}\frac{dp}{dx} = 0$$
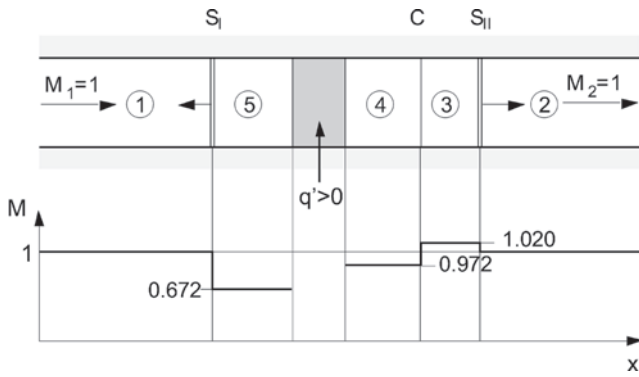
Fig. 11 Unsteady flow caused by heat addition exceeding Q_{max}, here $M_1 = 1 \rightarrow Q_{max} = 0$, $\gamma = 1.4$, instantaneous disturbance $q'/c_p T_{01} = 0.1$; S_I, S_{II} – upstream and downstream moving shock waves, respectively; C – contact surface (top); Mach number distribution (bottom)

and for the conservation of energy

$$c_p \frac{dT}{dx} + w \frac{dw}{dx} = \frac{dq}{dx}$$

or

$$-\frac{1}{\rho} \frac{d\rho}{dx} + \frac{1}{\gamma} \frac{1}{p} \frac{dp}{dx} = \frac{1}{c_p T} \frac{dq}{dx} \qquad (26)$$

Together with the differential equation of state

$$\frac{1}{p} \frac{dp}{dx} - \frac{1}{\rho} \frac{d\rho}{dx} - \frac{1}{T} \frac{dT}{dx} = 0 \qquad (27)$$

and known functions for $A(x)$ and $q(x)$, there are four equations for the four unknowns $w(x)$, $p(x)$, $\rho(x)$, and
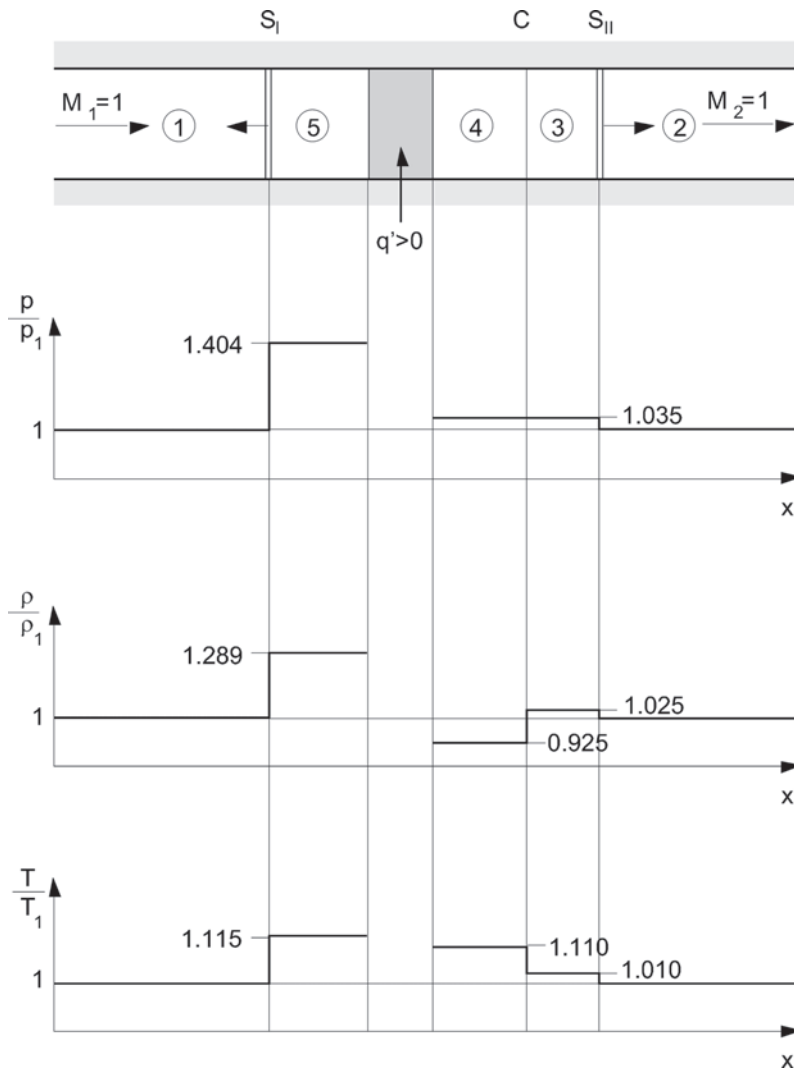

Fig. 12 Unsteady flow caused by heat addition exceeding Q_{max}, here $M_1 = 1 \rightarrow Q_{max} = 0$, $\gamma = 1.4$, instantaneous disturbance $q'/c_p T_{01} = 0.1$; pressure ratio p/p_1; density ratio ρ/p_1 and temperature ratio T/T_1 in the tube
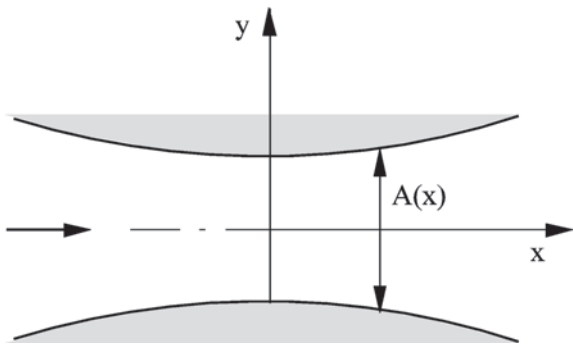
Fig. 13 Sketch of two-dimensional plane circular arc Laval nozzle with specified cross-sectional area $A = A(x)$

$T(x)$. For the corresponding differential equations

$$\frac{1}{w}\frac{\mathrm{d}w}{\mathrm{d}x} = -\frac{1}{1-M^2}\left\{\frac{1}{A}\frac{\mathrm{d}A}{\mathrm{d}x} - \frac{1}{c_pT}\frac{\mathrm{d}q}{\mathrm{d}x}\right\} \tag{28}$$

$$\frac{1}{\rho}\frac{\mathrm{d}\rho}{\mathrm{d}x} = \frac{1}{1-M^2}\left\{M^2\frac{1}{A}\frac{\mathrm{d}A}{\mathrm{d}x} - \frac{1}{c_pT}\frac{\mathrm{d}q}{\mathrm{d}x}\right\} \tag{29}$$

$$\frac{1}{p}\frac{\mathrm{d}p}{\mathrm{d}x} = \frac{\gamma M^2}{1-M^2}\left\{\frac{1}{A}\frac{\mathrm{d}A}{\mathrm{d}x} - \frac{1}{c_pT}\frac{\mathrm{d}q}{\mathrm{d}x}\right\} \tag{30}$$

$$\frac{1}{T}\frac{\mathrm{d}T}{\mathrm{d}x} = \frac{1}{p}\frac{\mathrm{d}p}{\mathrm{d}x} - \frac{1}{\rho}\frac{\mathrm{d}\rho}{\mathrm{d}x}$$

$$\frac{1}{T}\frac{\mathrm{d}T}{\mathrm{d}x} = \frac{1}{1-M^2}\left\{\frac{(\gamma-1)M^2}{A}\frac{\mathrm{d}A}{\mathrm{d}x} + (1-\gamma M^2)\frac{1}{c_pT}\frac{\mathrm{d}q}{\mathrm{d}x}\right\} \tag{31}$$

and with the definition of the Mach number $M = w/c = w/\sqrt{\gamma RT}$

$$\frac{1}{M}\frac{\mathrm{d}M}{\mathrm{d}x} = \frac{1}{w}\frac{\mathrm{d}w}{\mathrm{d}x} - \frac{1}{2T}\frac{\mathrm{d}T}{\mathrm{d}x}$$

$$\frac{1}{M}\frac{\mathrm{d}M}{\mathrm{d}x} = -\frac{1}{1-M^2}\left\{\left(1+\frac{\gamma-1}{2}M^2\right)\frac{1}{A}\frac{\mathrm{d}A}{\mathrm{d}x} - \frac{1+\gamma M^2}{2}\frac{1}{c_pT}\frac{\mathrm{d}q}{\mathrm{d}x}\right\} \tag{32}$$

Equation (32) demonstrates clearly the equivalent influence of $A(x)$ and $q(x)$ on compressible flows. However, due to the negative sign they act in the opposite direction. In comparison with isentropic nozzle flow, heat addition ($\mathrm{d}q/\mathrm{d}x > 0$) has an effect like a decrease of the geometrical cross-sectional area $A(x)$, i.e. acceleration in subsonic flow and deceleration in supersonic flow, which confirms our previously discussed equivalence of mass and heat addition. Only the influence of heat addition on the temperature gradient

changes its sign in a narrow range below Mach number 1. From equation (31) it follows that in subsonic flow for $M < 1/\gamma^{1/2}$ the second term in the braces tends to increase the temperature gradient. However, between $1/\gamma^{1/2} < M < 1$ this tendency is inverted and both terms in the braces tend to decrease the temperature gradient which is an interesting variation of the exchange between internal and kinetic energy in the transonic regime.

To solve the coupled system of equations (28) to (32), the temperature in equation (32) is eliminated by the energy balance

$$T = T_{01}\frac{1 + (q/c_pT_{01})}{1 + ((\gamma-1)/2)M^2} \tag{33}$$

After insertion into equation (32), the differential equation for the Mach number, only dependent on the known functions $A(x)$ and $q(x)$, is obtained

$$\frac{1}{M}\frac{\mathrm{d}M}{\mathrm{d}x} = \frac{1 + ((\gamma-1)/2)M^2}{M^2 - 1}$$
$$\times \left\{\frac{1}{A}\frac{\mathrm{d}A}{\mathrm{d}x} - \frac{1+\gamma M^2}{2(1+q/c_pT_{01})}\frac{\mathrm{d}(q/c_pT_{01})}{\mathrm{d}x}\right\} \tag{34}$$

2.2.2 Singularities and thermal choking

Aside of special cases, e.g. for heat addition at constant Mach number $M_q = $ const. or if $M \ll 1$ with isobaric supply, the transition from supersonic to subsonic flow and vice versa requires a careful analysis of the nature of the different singularities occurring in equation (34).

Assuming supersonic heat addition, the Mach number relatively or absolutely decreases towards sonic condition $M = 1$ (Fig. 14).
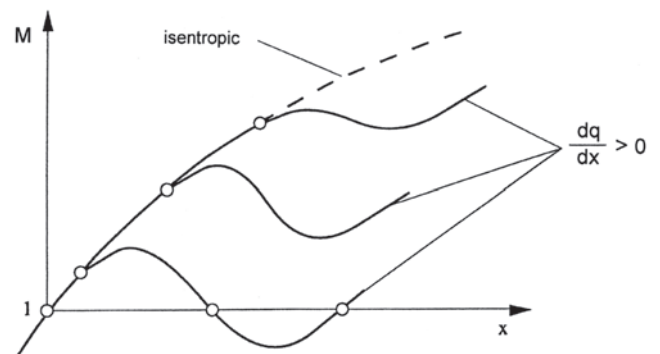

Fig. 14 Sketch of Mach number distribution in one-dimensional Laval nozzle flow with heat addition compared with the isentropic expansion; upper curves – pure supersonic heat addition; lower curve – supersonic heat addition with embedded subsonic region

If the Mach number approaches 1, the necessary condition for a finite gradient $(\mathrm{d}M/\mathrm{d}x)_{M=1} \neq \infty$ requires for the expression in the braces of equation (34)

$$\frac{1}{A}\frac{\mathrm{d}A}{\mathrm{d}x} - \frac{1+\gamma}{2}\frac{\mathrm{d}(q/c_\mathrm{p}T_{01})/\mathrm{d}x}{1+(q/c_p T_{01})} = 0$$

This means the gradient of the cross-sectional area $\mathrm{d}A/\mathrm{d}x$ of the Laval nozzle and the gradient of the heat addition $\mathrm{d}q/\mathrm{d}x$ must be properly adjusted, otherwise singularities cannot be avoided. If this severe condition is fulfilled, a steady flow solution with three sonic points and a local subsonic area embedded in supersonic flow regions are obtained (Fig. 16(f)).

Without exception, in flows with non-equilibrium condensation, the gradient of the instantaneous heat addition is always much greater than the area variation $\mathrm{d}A/\mathrm{d}x$. With

$$\frac{1}{A}\frac{\mathrm{d}A}{\mathrm{d}x} \ll \frac{1+\gamma}{2}\frac{\mathrm{d}(q/c_\mathrm{p}T_{01})/\mathrm{d}x}{1+(q/c_\mathrm{p}T_{01})}$$

this results in

$$\lim_{M\to 1}\frac{1}{M}\frac{\mathrm{d}M}{\mathrm{d}x} = -\infty$$

i.e. the flow becomes thermally choked (Fig. 15). For a more detailed mathematical theory of thermal chocking of quasi one-dimensional nozzle flow, see Delale et al. [5].

The integral curve starting at the reservoir and passing through the nozzle throat turns into the centre of a spiral. Steady throughflow requires a jump from the integral curve rolling up the spiral to the lower branch emerging from the spiral towards the nozzle exit. In classical gas dynamics and with the assumption of infinite thickness, this is an adiabatic normal shock. Behind this shock, due to the continuous heat addition, the flow accelerates and it establishes automatically the continuous transition through $M = 1$ and expands further to supersonic
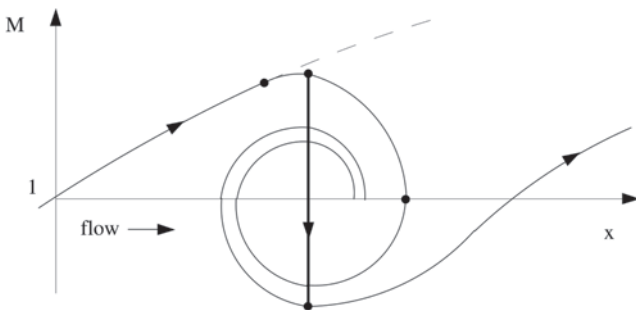

Fig. 15 Sketch of evolution of Mach number in steady Laval nozzle flow with supercritical heat addition and adiabatic shock
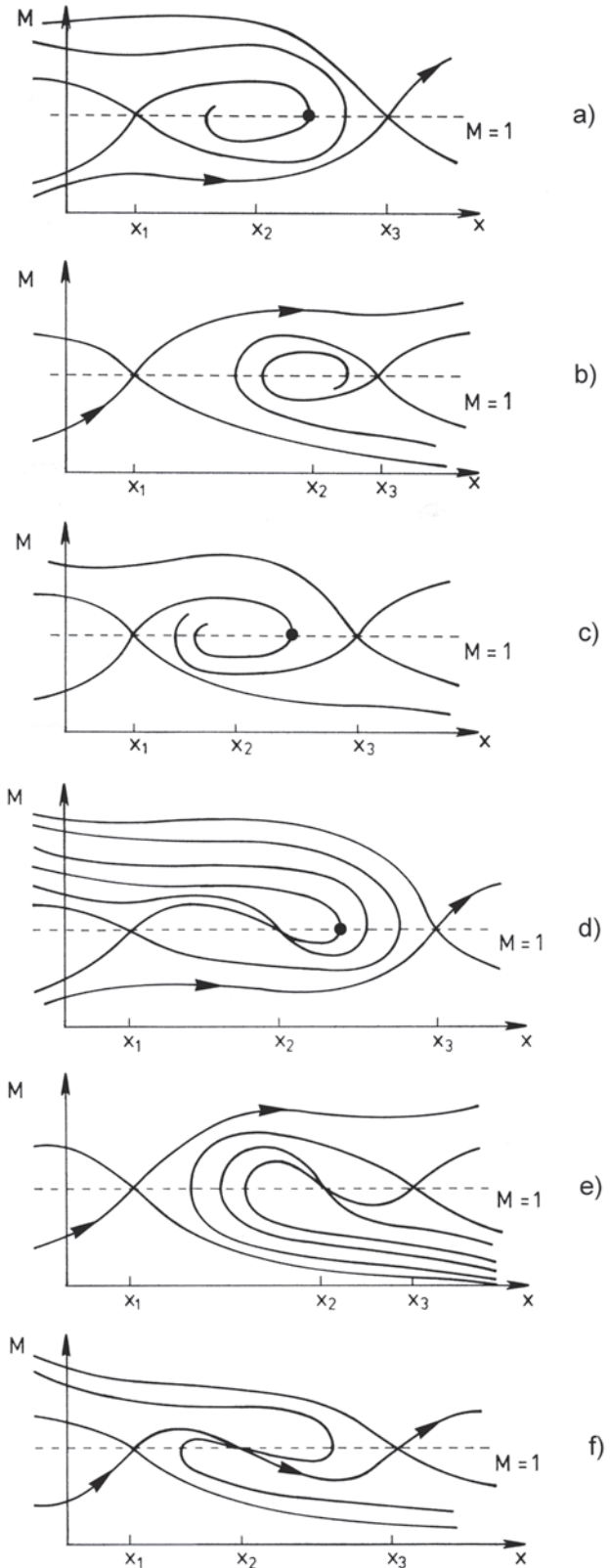

Fig. 16 Sketch of one-dimensional Laval nozzle flow with heat addition; summary of qualitative solutions consisting of saddle points, nodal points, and with spirals; original picture of Möhring [6]

Mach numbers according to the specified low pressure p_e at the nozzle exit.

This discontinuous flow is characterized with a steady shock just after the onset of heat addition as flow with supercritical heat addition. Here the topology of the solution consists of three singularities: the classical adiabatic saddle point at the nozzle throat, the spiral, and a second saddle point where the flow accelerates again to $M > 1$.

Möhring [6] investigated analytically all singularities of equation (34) at $M = 1$ for Laval nozzle flow with specified heat addition by assuming reasonable analytical expressions for $A(x)$ and of $q(x)$ – supersonic heat addition only. After local linearization of equation (34) in the vicinity of the singularities, the discussion of the characteristic homogeneous differential equation yields all possible trajectories emerging from the singular points. Figure 16 shows the qualitative results consisting of saddle points, nodal points, and spirals. In Fig. 16, the position of x_1 marks the location of the nozzle throat characterized by a saddle point singularity as know from isentropic flow. At x_2 the topology consists of spirals or nodal points, completed by saddle points at x_3 and qualitative trajectories in between. In the first example (Fig. 16(a)), the flow remains subsonic at the throat and behind to some extent. Owing to heat addition, it accelerates in the divergent nozzle regime to supersonic Mach flow creating an effective throat with $M = 1$. This topology is typical for strong supersonic heat addition (see numerical example in Fig. 19). Figure 16(b) represents the opposite case. Here the flow accelerates adiabatically through the throat to $M > 1$ and the supersonic heat addition deforms the trajectory only a little bit (see calculated result

in Fig. 17). This type corresponds to the weak solution respectively to subcritical heat addition. In Fig. 16(c), there exists no single trajectory starting at $M < 1$ and connecting with the regime $M > 1$. However, if a normal shock links the upper branch of the spiral with the lower one, this type represents diabatic flow with supercritical heat addition (for comparison, see the numerical example in Fig. 18). Figures 16(d) and (e) belong to similar steady diabatic flows as shown by Figs 16(a) and (b). The type of singularity appearing at x_2 depends mainly on the gradients of $A(x)$ and $q(x)$. The lowest picture (Fig. 16(f)) depicts the interesting configuration with continuous compression back to subsonic flow according to the necessary condition of simultaneous vanishing numerator of equation (34) at $M = 1$, realized by a nodal point between two saddle points.

2.2.3 Numerical examples

Figures 17 and 18 show numerical examples, assuming a slightly curved two-dimensional plane circular arc nozzle with a cooling rate $-\mathrm{d}T/\mathrm{d}t \approx 0.4\ \mathrm{K}/\mu\mathrm{s}$ (nozzle No. 8 – see Table 1). The chosen analytical function $q(x)$ for the heat addition is quantitatively representative for non-equilibrium condensation of water vapour mixed in carrier gas, starting from a reservoir with $T_{01} = 293$ K and $p_{01} = 1$ bar [7].

The first result represents the continuous or subcritical flow type (Fig. 16(b) of Möhring's topology) with isentropic acceleration through the geometrical nozzle throat and a weak supersonic compression after the onset of heat addition. The spiral between the two saddle points deforms this integral curve
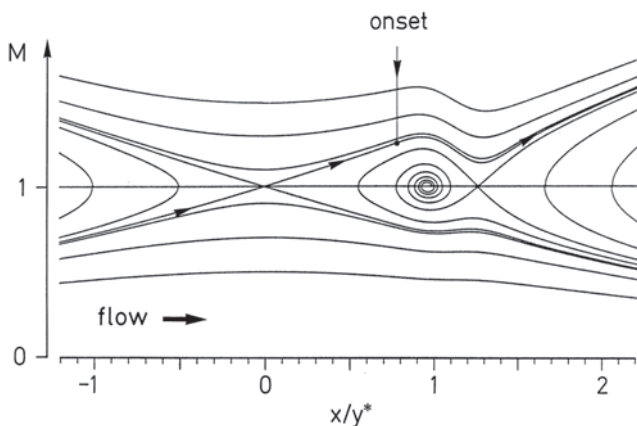

Fig. 17 Continuous Laval nozzle flow (nozzle No. 8 – see Table 1) with isentropic acceleration through the throat and weak supersonic compression after onset of subcritical heat addition at onset Mach number $M_{\mathrm{onset}} = 1.257$ – numerical result
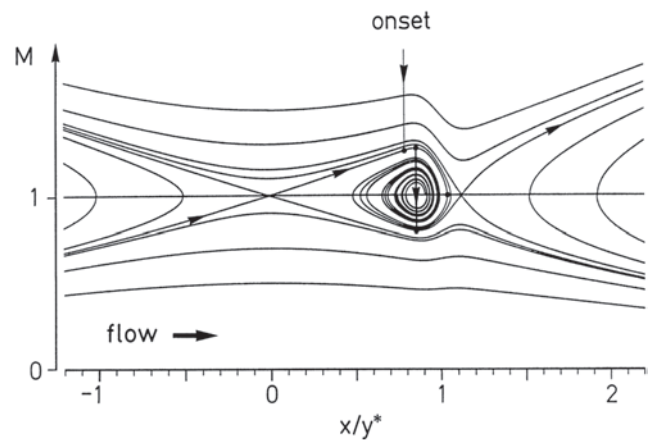

Fig. 18 Laval nozzle flow (nozzle No. 8 – see Table 1) with supercritical heat addition and steady normal shock for the same onset Mach number $M_{\mathrm{onset}} = 1.257$ but a slightly steeper gradient of the specified function $q(x)$ – numerical result

Table 1 Geometric data and cooling rates of two-dimensional, axisymmetric nozzles under consideration

Nozzle	y^* (mm)	R^* (mm)	y^*/R^*	$\left(-\dfrac{\mathrm{d}T}{\mathrm{d}x}\right)^*_{\text{one-dimensional 293 K}}$ (K/cm)	$\left(-\dfrac{\mathrm{d}T}{\mathrm{d}t}\right)^*_{\text{one-dimensional 293 K}}$ (K/μs)
2	30	100	0.3000	11.51	0.33
3	60	200	0.3000	5.76	0.16
4	15	400	0.0375	8.14	0.23
5	30	200	0.1500	8.14	0.23
6	60	100	0.6000	8.14	0.23
7	30	584	0.0514	4.76	0.14
8	20	127	0.1575	12.51	0.36
A1	45	300	0.1500	5.43	0.16
A1A	45	300	0.1500	5.43	0.16
A1 3D	45	300	0.1500	7.68	0.22

only a little bit behind the given onset of heat addition at the onset Mach number $M_{\text{onset}} = 1.257$.

For the same onset Mach number $M_{\text{onset}} = 1.257$ and the same maximum amount of the added heat but for a slightly steeper gradient $\mathrm{d}q/\mathrm{d}x$ of the prescribed analytical function $q(x)$, the flow immediately becomes supercritical with a steady normal shock (Fig. 18). Here the steady flow solution is found by an iterative technique to fit an adiabatic normal shock between the two branches of the spiral. By avoiding thermal choking, this shock enables steady flow close to the limit of stability. By definition, this shock does not alter the specified heat distribution $q(x)$.

This second example reveals important characteristics and similarities with condensing flows with steady shocks. Typically the onset of heat addition and the shock location are very close together. This indicates that there exists only a very limited range for stabilization of such flows by a normal
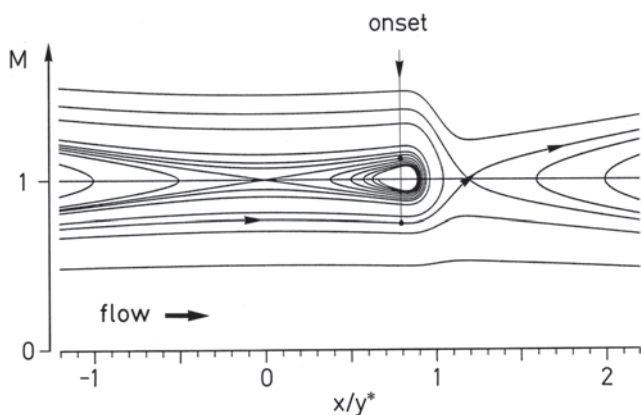

Fig. 19 Laval nozzle flow (nozzle No. 8 – see Table 1) with heat addition and for the same onset Mach number $M_{\text{onset}} = 1.257$, but with further steepened gradient of the specified function $q(x)$ – numerical result. Shock fitting is not possible, the topology rearranges to subcritical heat addition with $M < 1$ at the nozzle throat

shock. If a shock could successfully be inserted into this flow topology, the amount of added heat ahead of this shock is very low, only a few per cent, typically less than 2–3 per cent of the maximum amount of heat available. This means that in the supercritical case approximately all heat is supplied downstream of the shock. The position of the shock close to the onset of macroscopic heat addition is important for understanding the reaction of shocks on vapour flows with nucleation and droplet growth. This means that in this case the shock locates only a bit downstream of the so-called Wilson point with maximum supersaturation and it decreases the growth of the smallest droplets only by decreasing the supersaturation, but the temperature increase is not as much that it could cause de-nucleation. Therefore, a steady shock in condensing flow causes a change of the gradient of the growth of the condensate mass fraction g (discussed later).

If the gradient of the given heat supply $q(x)$ is further increased, with constant onset Mach number and the same maximum amount of heat as before, the trial for shock fitting fails, meaning that the analytical normal shock condition can no longer be fulfilled and the topology between the singularities changes (Fig. 19). The second singularity is still a spiral, but no shock can be fitted between the oncoming integral curve which accelerates to $M = 1$ at the geometrical throat at $x/y^* = 0$ and rolls up into the centre and any other integral curve connected with the nozzle exit. This means that no steady throughflow exists under these conditions with $M = 1$ at the nozzle throat ($x/y^* = 0$).

Nevertheless, there are several integral curves that clearly represent steady-state solutions but with subsonic flow at the throat ($x/y^* = 0$). For instance, if the subsonic Mach number is approximately constant (i.e. 0.75) till the onset of heat addition then, driven by the heat addition, the flow accelerates in the divergent nozzle part to $M = 1$ and continuously to supersonic flow towards the prescribed low pressure at the nozzle exit. In other words, the equivalent displacement effect of the heat addition forms in the

divergent nozzle part an effective minimum cross section [1, 2] and yields critical flow conditions with $M = 1$ far behind the onset heat addition. This is exactly what equation (31) expresses as necessary condition if $M \to 1$ and if the gradients of dA/dx and dq/qx balance each other. What is interesting to note here is that a previously steady-state super-critical flow pattern changes into another steady-state solution with subcritical heat addition. This result corresponds to Fig. 16(a) of Möhring's topology.

Thus, instantaneous increase of the gradient of a specified heat addition $q(x)$ in steady diabatic nozzle flow as shown in Fig. 18 causes pressure waves that monotonically decrease the oncoming Mach number ahead of the onset of heat addition till a new subcritical steady-state solution establishes according to Fig. 19. Obviously, this disturbance causes a transient switch from one initially steady-state configuration to another steady-state solution but no oscillatory dynamics or self-excitation develops.

In conclusion, self-excitation with periodic oscillations is only possible if the physical nature of the phase transition process and the two-way coupling with the diabatic compression waves and shocks are included in the flow model.

3 SELF-EXCITED PERIODIC INSTABILITIES

3.1 Mechanism of self-excitation

We have already seen how monotonic unsteady waves develop in constant-area flow after instantaneous addition of heat exceeding the threshold value Q_{max}. However, at initial steady vapour flow with $A = $ const., i.e. at constant pressure and temperature, there is no driving potential for phase transition with nucleation and droplet growth. Thus, from this flow model unsteady phenomena are not to be expected after replacing the fluid by a condensable vapour or vapour/carrier gas mixture. Self-excitation in condensing flows requires gradients of pressure and temperature with acceleration, subcooling and supersaturation, and is therefore only possible at initial steady flow with varying cross-section.

If the heat addition is coupled to the flow in both directions, i.e. if heat is released to the flow after onset of condensation and if this latent heat release initiates pressure waves according to our previous model, the upstream travelling waves and the related temperature increase interact with the condensate consisting of very small droplets. This reduces the supersaturation and therefore the nucleation rate. The reduction of the nucleation rate results in a decrease of the growth rate of the condensate mass fraction. In other words, the compression waves, caused by the latent heat addition itself, tend to decrease the driving mechanism of the heat release instantaneously and therefore the heat release itself. Then instantaneously expansion waves tend to re-establish the adiabatic Mach number distribution according to the specified area $A(x)$, the flow accelerates to $M = 1$ close to the throat and to supersonic flow further downstream. But now the supersaturation increases and the nucleation process intensifies again, a new supercritical shock forms and the following period of the self-excitation mechanism starts. In a given Laval nozzle, the frequency of this self-excited oscillation is controlled by the condensable vapour mass content. Typical frequencies are of the order of 1 kHz. Relevant aspects of this interesting dynamical phenomenon will be discussed in the following sections.

3.2 Physical modelling of the condensation process

The formation of droplets in supercooled vapour is considered by the nucleation theory. Reviews of the kinetic and statistical mechanics' approaches to the theory are presented in this issue by Bakhtar *et al.* [8] and by Ford [9], respectively. Therefore, it is repeated here only a few details that are necessary for understanding of this what follows. All computational fluid dynamics (CFD) simulations presented here are based on the classical nucleation theory of Volmer [10] and Frenkel [11]. It is obvious that this steady-state capillary theory is problematical if the critical nuclei radii are of the order of 10^{-9} m and for applications with high-frequency oscillations as typical for transonic flows under consideration. However, if macroscopic gas dynamic effects, i.e. the integral effects, are in focus and if quantitative accurate determination of local nucleation rates at each instant and at each location in the flow field is not the main concern, all experience based on detailed comparison with experiments confirms the convincing capability of this classical theory. Among the many existing modifications of the classical nucleation theory, the revised models of Dillmann and Meier [12] and of Lamanna [13] show excellent quantitative agreement with measured nucleation rates in steady and unsteady flows, respectively. Depending on the application, pure homogeneous nucleation or simultaneous homogeneous/heterogeneous nucleation on pre-existing solid particles, simulating natural impurities, or artificial seeding, together with appropriate droplet growth models, is investigated. Quantitative data of the *a priori* unknown microscopic model parameters

have to be determined by detailed comparison with experiments based on measurements of pressure and density, and on flow visualizations. Comparing the characteristic frequency for formation of critical nuclei indicates that the steady-state nucleation theory is still appropriate for simulation of unsteady flows in the frequency range of the order of 1 kHz.

The existence of carrier does not change the principal characteristics of condensation dynamics in compressible flow, including the formation of instabilities. However, it is clear that fluid properties such as specific heat ratio and latent heat control the diabatic effects, and the operating conditions vary depending on the nature of the working fluid as pure vapour or as mixture of vapour and carrier gas. Mosnier [14] investigated oscillations in Laval nozzles with the focus on the influence of the specific heat ratio. Experiments were carried out in a Ludwieg tube with emphasis on water vapour condensation depending on the nature of the carrier gas. Mono-atomic carrier gases tend to shift the onset of condensation towards subsonic flow. As experimental investigation including visualization of such flows in indraft wind tunnels is much easier under atmospheric temperature conditions, instead of operating with superheated vapour, most of the experiments available in the literature deal with humid air and are therefore used here for explaining the physical nature of the topology of self-excited instabilities of condensing flows.

3.3 Self-excited oscillations in Laval nozzles

The phenomenon of self-excited oscillations in condensing nozzle flows has been discovered by Schmidt [15] performing experiments in a small atmospheric indraft wind tunnel. Barschdorff [16] performed the first quantitative experiments for investigation of the frequency dependence by using the same test facility. Figure 20 shows a sequence of one cycle in the slender circular arc nozzle No. 7 ($y^* = 30$ mm, $R^* = 584$ mm – see Table 1) used for this pioneering work. The fluid is humid air of $\phi_0 = 83$ per cent and $x = 9.5$ g$_{vapour}$/kg$_{dry\ air}$.

The isochoric structure of the flow is visualized here using Mach–Zehnder interferometry and a high-speed Strobodrum camera; the Mach–Zehnder interferometer is adjusted with finite fringe width. The flow direction is from left to right, time starts at the left column on top. At left in the converging nozzle part, a discontinuity moving into the oncoming flow is observed; this is the for-runner shock of the previous period. At the right side of the throat, a weak disturbance builds up, steepens while moving towards the throat and forms the new shock of the following period, here with a frequency of 749 Hz.
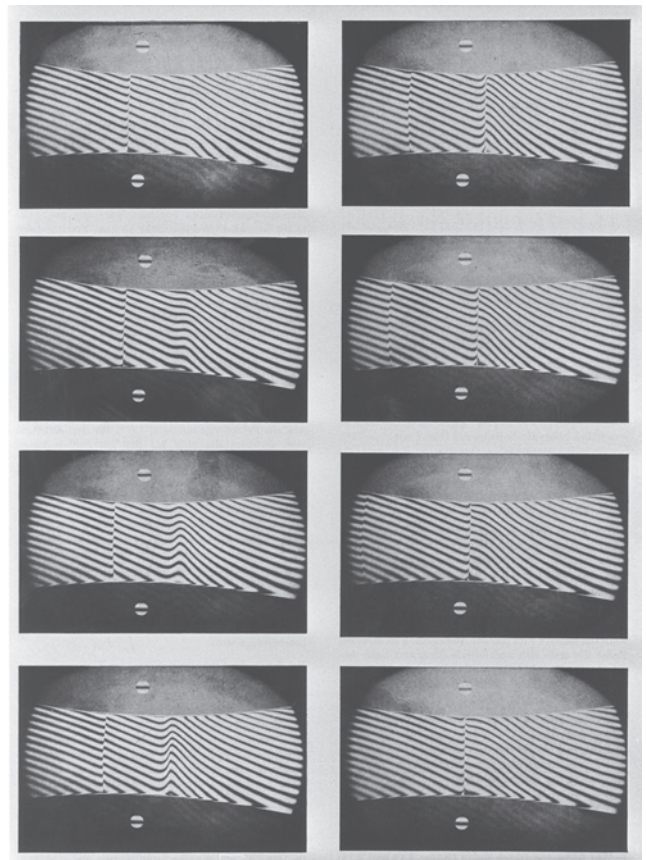

Fig. 20 Mach–Zehnder interferograms of one periodic cycle of self-excited oscillations of condensing flow in nozzle No. 7 (see Table 1), flow from left, starting at left column from top; frequency $f = 749$ Hz; indraft wind tunnel experiment, operating with atmospheric humid air, reservoir conditions: $\phi_0 = 83\%$, $x = 9.5$ g$_{vapour}$/kg$_{dry\ air}$, original picture from Barschdorff [16]

Figure 21 shows a Schlieren sequence of the same phenomenon in the circular arc nozzle No. 4 ($y^* = 15$ mm, $R^* = 400$ mm – see Table 1) and for reservoir conditions $\phi_0 = 91$ per cent and $x = 12.2$ g$_{water\ vapour}$/kg$_{mixture}$ [17]. In both examples, the shock forms in transonic/supersonic flow in the right-hand divergent nozzle part. It moves upstream, passes through the throat, accelerates, and dies out in subsonic flow. This shock does not oscillate. It moves monotonically opposite to the main flow direction. Here the frequency is significantly higher, i.e. $f = 1145$ Hz. The relevant part of the flow regime is transonic and the latent heat release tends to establish a supercritical shock. This shock does not find a steady-state position and initiates self-excitation as discussed in the previous section.

The first numerical simulations of unsteady two-phase flows with non-equilibrium condensation of
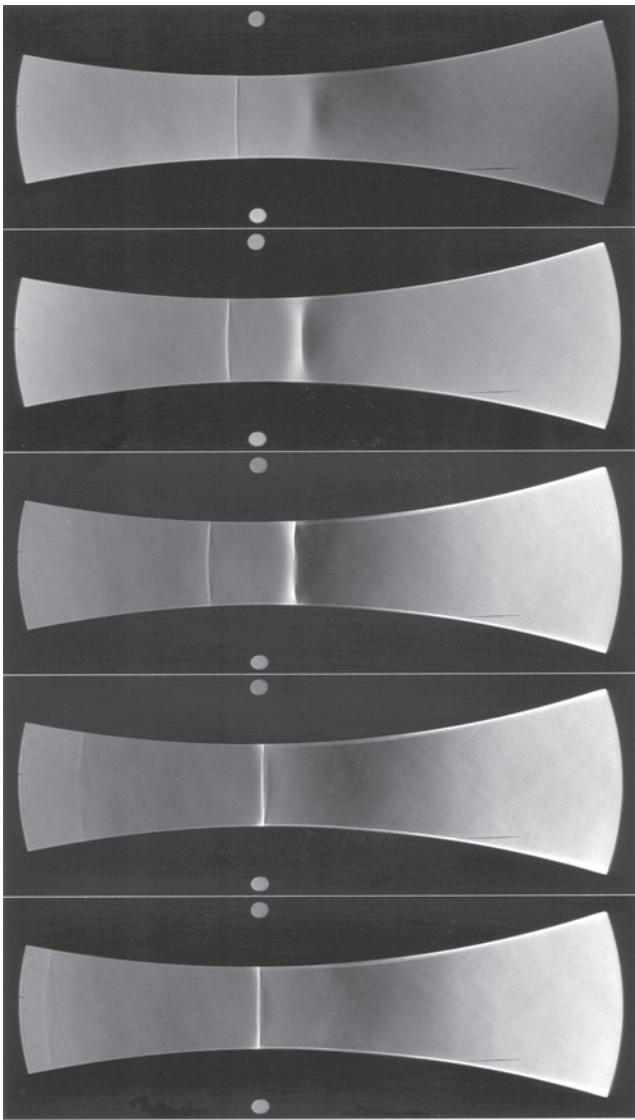
Fig. 21 Schlieren pictures of self-excited shock formation in nozzle No. 4 (see Table 1), flow from left; frequency $f = 1145$ Hz; indraft wind tunnel experiment, operating with atmospheric humid air, reservoir conditions: $T_{01} = 291.65$ K, $p_{01} = 1.0$ bar, $\phi_0 = 91.0\%$, $x = 9.5$ $g_{vapour}/kg_{dry\ air}$

An important step towards realistic simulations of complex technical flows was the first two-dimensional calculation of unsteady wet steam flow by White and Young [21], based on the preceding numerical investigation of Guha and Young [22]. Mundinger [23] developed an effective scheme to calculate unsteady, homogeneously condensing flows including carrier gas effects. Young [24] provided the fundamental equations for accurate calculation of gas-droplet multiphase flows. The numerical results presented in this article have been obtained using the vectored scheme described by Schnerr and Dohrmann [25] and by Adam and Schnerr [26].

Figure 22 shows details of a numerical simulation of the experiment according to Fig. 21 for the same nozzle No. 4 and approximately the same reservoir conditions. The first column at left-hand side depicts the pressure waves and the moving shock.

If the shock enters the nucleation zone, it instantaneously reduces locally the peak value of the nucleation rate J (second column). This interaction intensifies rapidly and reaches a maximum when the shock passes through the throat (Fig. 22, second column, picture 3 from top). Quantitatively, the peak value of the nucleation rate J decreases at this instant from 10^{23} to 7×10^{18} m^{-3} s^{-1}. This decreases the latent heat release instantaneously, and further downstream a tremendous nuclei formation sets in (picture 4 from top). The corresponding condensate formation, together with the related heat release (third column), immediately produces compression waves that steepen again, and finally the next shock builds up and interacts with the nucleation process. Figure 23 illustrates this dynamical process following a streamline along the nozzle axis for the nucleation rate J, the condensate mass fraction g/g_{max}, and the normalized static pressure ratio p/p_{01}.

It should be noted that the formation of the new phase at the microscopic scale is clearly two-dimensionally structured, even in this very slender quasi-one-dimensional nozzle. This emphasizes the sensitivity of the nucleation process for smallest variations of thermodynamic variables.

3.3.1 Symmetric instabilities

3.3.1.1 Frequency dependence of quasi-one-dimensional flow. All results in the previous chapter were obtained with nozzles having small values of the wall curvature parameter y^*/R^*, e.g. for nozzle No. 4, $y^*/R^* = 15/400 = 0.0375$ and for nozzle No. 7, $y^*/R^* = 30/584 = 0.0514$. To avoid any additional complication caused by two-dimensional wave phenomena, the following discussion of the frequency dependence is restricted on such slender nozzles.
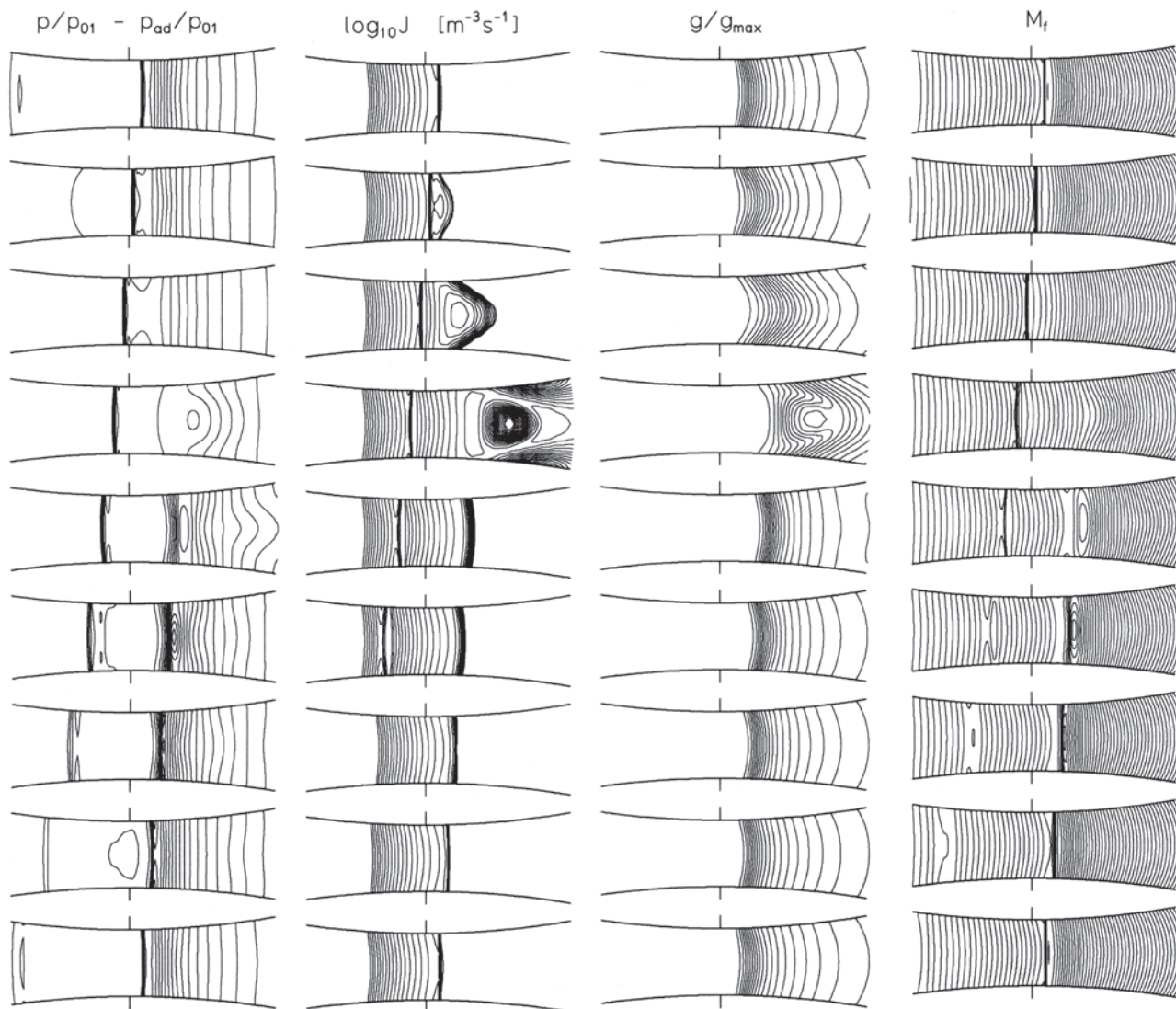
water vapour were presented by Saltanov and Tkalenko [18]. They applied an extended Gudunov method to solve the one-dimensional Euler equations coupled with the classical nucleation theory of Frenkel. The theoretical treatments of two-dimensional two-phase flows of steam and comparison with cascade measurements are reviewed in this issue by Bakhtar *et al.* [19]. An investigation of unsteady flows of nucleating steam in a convergent–divergent nozzle using a one-dimensional treatment based on MacCormack's scheme is described by Skillings and Jackson [20].

Fig. 22 Inviscid numerical simulation of one cycle of self-excited oscillations of condensing flow from left in nozzle No. 4 – unsteady interaction of upstream moving shock with static pressure, nucleation rate, condensate mass fraction, and frozen Mach number – from left; frequency $f = 1122$ Hz; atmospheric humid air, reservoir conditions: $T_{01} = 295.0$ K, $p_{01} = 1.0$ bar, $\phi_0 = 90.0\%$, $x = 15.02$ $g_{vapour}/kg_{dry\ air}$

Figure 24 collects the original data of the experiments of Barschdorff (see, e.g. the interferograms of Fig. 20); it depicts the frequency dependence on the mixing ratio x ($g_{vapour}/kg_{dry\ air}$) for two different nozzles (Nos 5 and 7). The important difference of the nozzles No. 5 and 7 is the temperature gradient, $(-dT/dx)^*_{one-dimensional} = 8.14$ K/cm for nozzle No. 5 and $(-dT/dx)^*_{one-dimensional} = 4.76$ K/cm for nozzle No. 7. Barschdorff found the limit of one-dimensional stability between $x = 8$ and 9 g/kg. In one and the same nozzle, the frequency increases with the mixing ratio. This is quite obvious, because a larger amount of condensate initiates stronger pressure waves and therefore faster moving shocks. Similar

results of unsteady condensing nozzle flows are reported by Matsuo *et al.* [27].

Figure 24 shows also that the frequency increases with the temperature gradient or with the acceleration in the nozzle. The reason is the decrease of the amplitude of the shock motion in nozzles of higher gradients, although this effect yields higher condensation onset Mach numbers what tends in opposite direction. These original data indicate a monotonic increase of the frequency with relative humidity ϕ_0 of the upstream reservoir including the region near the limit of stability. More careful investigations of this subject showed that this is only true at the right-hand side of a sharp frequency minimum. At
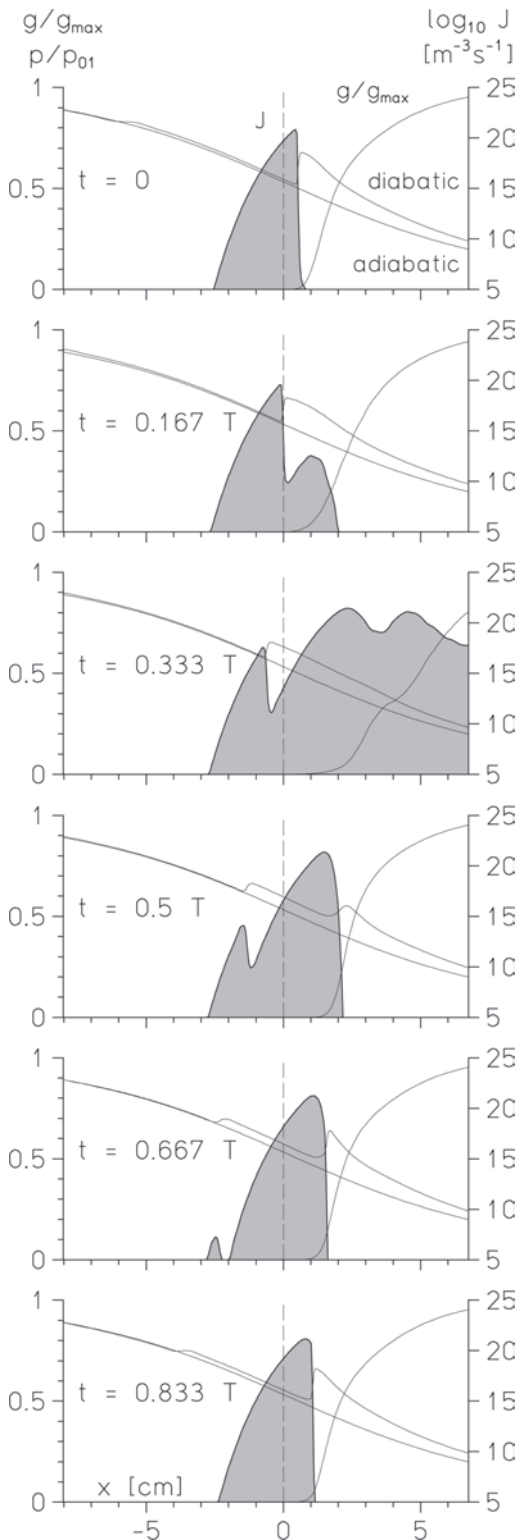
Fig. 23 Periodic oscillation in nozzle No. 4 corresponding to Fig. 22; time increases from top, throat position at $x = 0$; pressure ratio p/p_{01}, normalized condensate mass fraction g/g_{max} and nucleation rate J $(m^{-3} s^{-1})$ (shaded area) at the nozzle axis; the lower expansion curve starting at the ordinate at left depicts the steady-state isentropic expansion
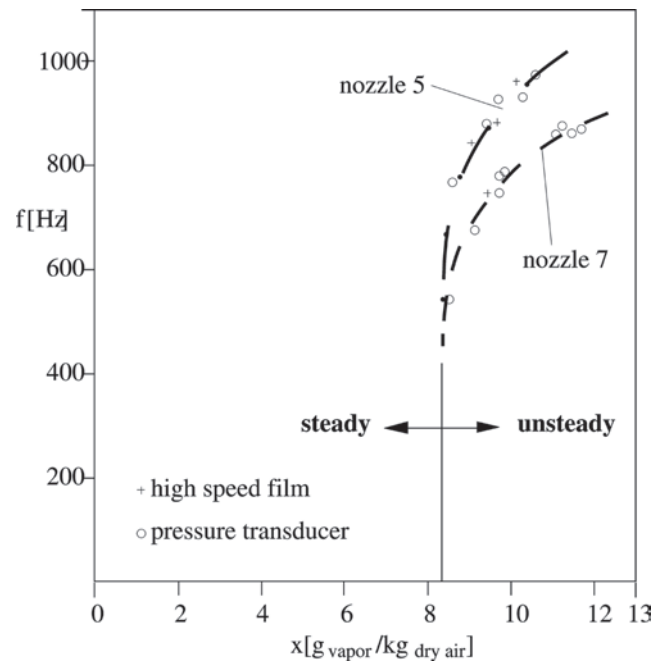

Fig. 24 Influence of the mixing ratio x $[g_{vapour}/kg_{dry\ air}]$ on the frequency of self-excited oscillations for approximately constant reservoir values of temperature T_{01} and pressure p_{01} according to Barschdorff [16]; indraft wind tunnel experiment, humid air, nozzle No. 7 – $T_{01} \approx 290.0$ K, nozzle No. 5 – $T_{01} \approx 286.0$ K

left of this minimum, the opposite tendency prevails; here the frequency decreases rapidly with increasing relative humidity ϕ_0 of the upstream reservoir. The numerical result of Fig. 25 calculated for nozzle No. 4 with $y^*/R^* = 0.0375$ is well confirmed by experiments including the existence of the minimum [28]. Topology of the frequency variation of these experimental and numerical results are in excellent agreement with the pioneering experiments [29].

From Schlieren streak registrations it is evident that the frequency minimum separates two dynamical modes of the moving shock. Mode 1 (Figs 25 and 27(a)), already discussed before, corresponds to the branch with increasing frequency at the right-hand side of the minimum. At left of the minimum, the shock still forms in supersonic flow, moves upstream but it does not pass through the throat. Ahead of the throat it decelerates, stops, reverses, and moves downstream in main flow direction. Then it dies out before it returns to its origin – mode 2 (Fig. 27(b)). At the same time a new shock builds up. Obviously, the moving shock performs an incomplete oscillation in the right-hand nozzle part and the oncoming flow ahead of the throat remains in steady state. The sharp minimum corresponds exactly to the situation when the upstream
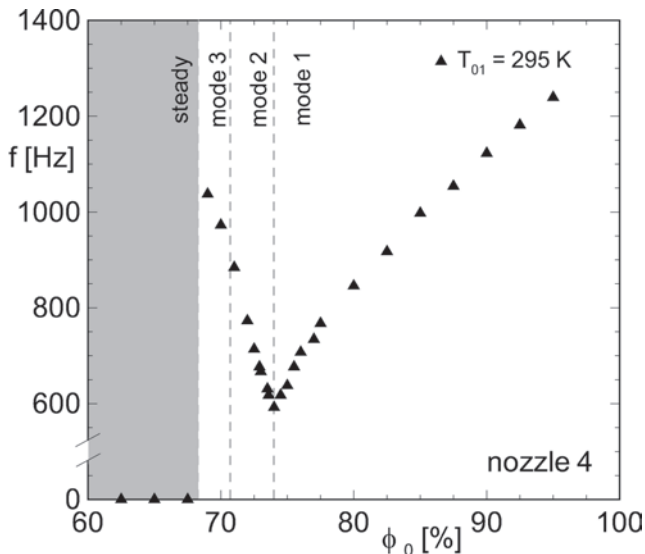
Fig. 25 Influence of the water vapour pressure ratio ϕ_0 on the oscillation frequency f for constant reservoir temperature $T_{01} = 295.0$ K and pressure $p_{01} = 1.0$ bar; humid air, nozzle No. 4 – inviscid numerical simulation

moving shock just stops at the throat at $M = 1$. As distinguished from mode 1, there is no periodic variation of the oncoming mass flux that is an important aspect for technical applications.

The sketch of Fig. 26 depicts the Schlieren streak arrangement to register the shock motion along the nozzle centerline. The flow field in the area of a narrow slit at the nozzle axis is projected onto a high-speed movie. Superposition of shock and film motion yields the time-dependent shock location including the local strength and frequency of the shock (Figs 27(a) to (c)).

Concerning the condensate formation, modes 1 and 2 behave significantly different. As the shock decelerates and stops instantaneously, there is a much stronger interaction of the temperature increase through the shock with the nucleation process. The time-dependent mean value of the condensate mass $\bar{g}$ ($g_{liquid}/kg_{mixture}$) at the nozzle exit depicts individual profiles, different in depth and width according to the modes (Fig. 28); $\bar{g}/g_{max}$ is the, at the nozzle exit plane, area-averaged mean value of the non-dimensional condensate mass fraction at each instant of one oscillation period with T as the time of one period. According to the strongest interaction of shock and nucleation, the maximum reduction of the liquid phase is observed in oscillations of mode 2 (Fig. 27(b)).

Figure 27(c) shows the third mode of oscillation for supply conditions just a little bit above the stability limit – mode 3. Now the shock oscillates periodically with approximately constant strength and small
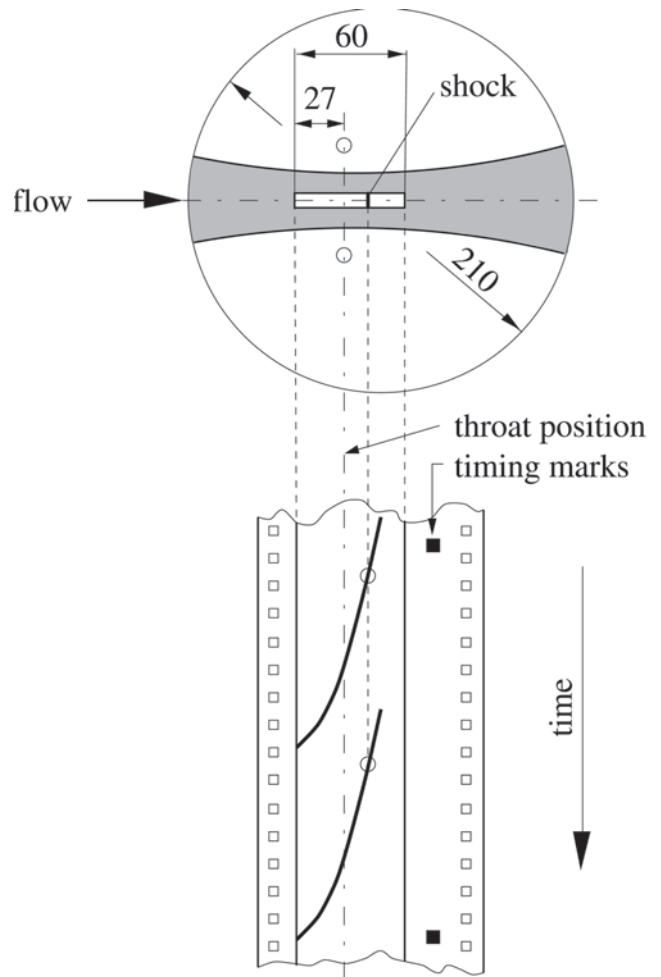

Fig. 26 Sketch of Schlieren streak technique for high-speed registration of moving shocks

spatial amplitude in the divergent nozzle section close to the limiting shock position of the steady flow regime. The frequency of 956 Hz is typically as high as that of mode 1 but the amplitude of the shock motion is much smaller in comparison to the other modes 1 and 2.

Barschdorff [30] performed further experiments using his slender nozzle No. 7 but operating with pure steam instead of humid air. In principle, the same instability was observed. Figure 29 shows three interferograms of the self-excited formation of unsteady moving shocks in steam flow for the following reservoir conditions: $T_{01} = 480$ K, $p_{01} = 1.16$ bar. The resulting frequency of this instability of mode 1 ($f = 801$ Hz) is of the same order as found in experiments operating with mixtures of water vapour and carrier gas. The existence of a distinct frequency minimum is further confirmed by numerical investigations of homogeneously condensing pure vapour flows [31].

So far, the existence of carrier does not change the principal characteristics of these instabilities.
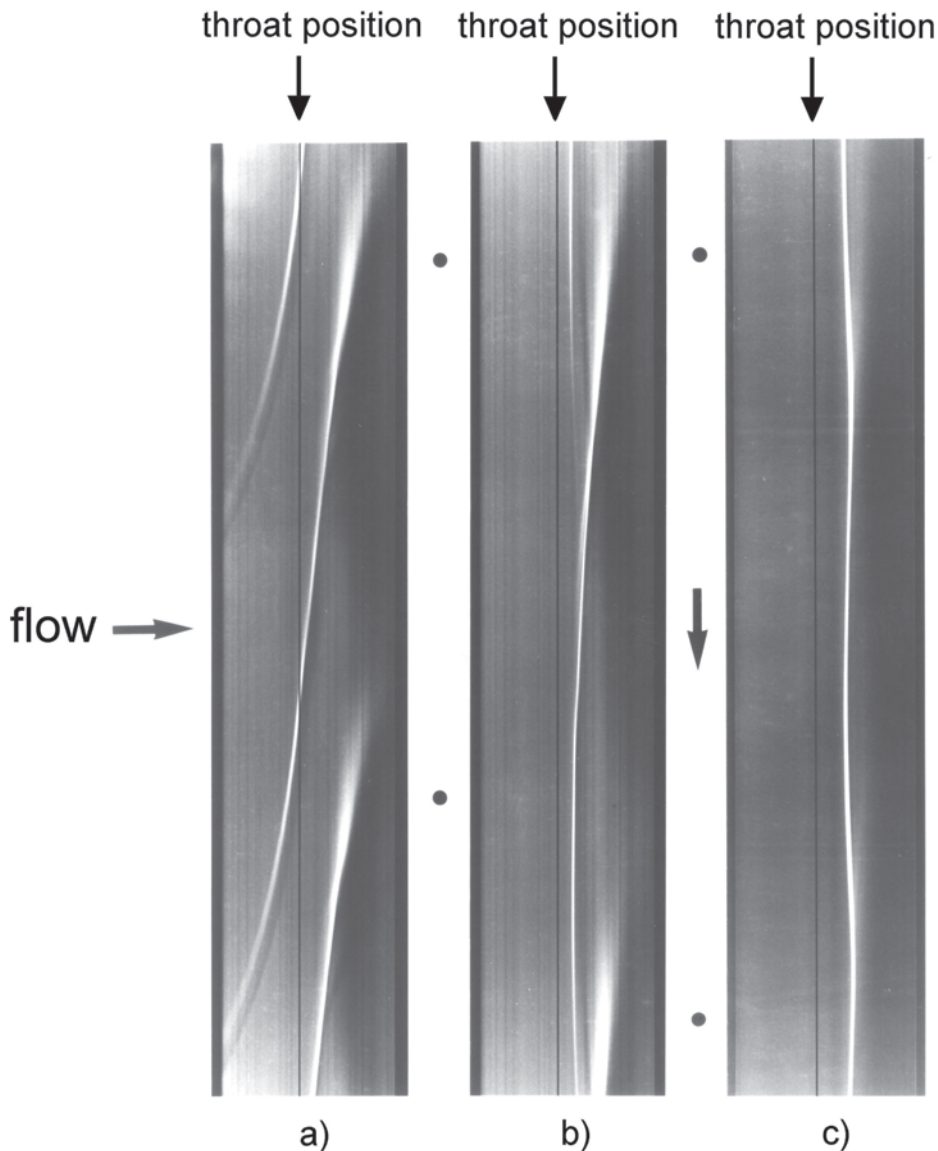
throat position   throat position   throat position

flow →

a)   b)   c)

Fig. 27 Schlieren streak registration of self-excited periodic shock formation/oscillation in circular arc nozzle No. 4 (time increases from top, flow from left). The vertical black line indicates the location of the nozzle throat, the dots represent the interval of one period

However, reservoir conditions and supersaturation vary depending on the nature of the working fluid as pure vapour or as mixture of vapour and carrier gas.

The first similarity law for the oscillation frequency of this first-order instability was derived by Zierep and Lin [32] based on the wind tunnel experiments of Barschdorff operating with humid air. At Yale University, Wegener and Cagliostro [33] and Wegener and Mosnier [34] performed detailed experiments using a Ludwieg tube and reported a dimensional analysis of all essential variables including a stability diagram for different nozzle shapes and carrier gas influence. Sichel [35, 36] from the same group at Yale developed a theory for description of unsteady transonic flow with heat addition based on the

assumption of isentropic and irrotational flow, i.e. the small disturbance potential equation. Petr [37] considered the stability of a diabatic shock theoretically. Delale *et al.* [38] recently derived a mathematical theory including a theoretical condition for the limit of stability of a supercritical shock based on asymptotic approach.

3.3.1.2 Wall curvature effects. What changes if curvature effects are more intense? In flows with strong streamline curvature, the highest supercooling and the onset of heat addition locate at the nozzle walls with maximum curvature. In transonic/ supersonic flow, all pressure and temperature disturbances evolve from there along characteristics. These waves interfere with the phase transition
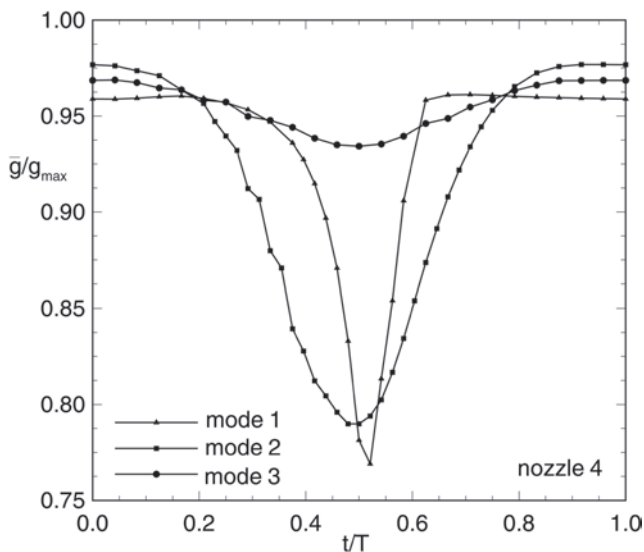
Fig. 28 Nozzle No. 4, time-dependent area-averaged mean value of the normalized condensate mass fraction $\bar{g}/g_{max}$ at the nozzle exit for modes 1, 2, and 3

process, which is controlled by thermodynamics and therefore triggered by iso-lines or iso-surfaces of constant temperature, and stabilize the flow via the so-called subsonic heating fronts to remain in steady state [39]. To demonstrate this effect, the dynamical behaviour of oscillations in nozzles No. 4, 5, and 6 where $(-dT/dt)^*_{one\text{-}dimensional}$ is kept constant but the curvature parameter y^*/R^* varies more than one order from 0.0375 to 0.6 is compared Fig. 30).

Although the cooling rates are kept constant, the frequency response for identical reservoir conditions is completely different, e.g. for $T_{01} = 295$ K the stability limit moves from $\phi_0 = 68$ per cent for nozzle No. 4 to $\phi_0 = 74$ per cent for nozzle No. 6. As the main effect, there exists no such distinct frequency minimum as shown for quasi-one-dimensional nozzles. In strongly curved nozzles, the instability separates from the walls and restricts locally to a narrow range around the nozzle axis. However, near the walls the approximately steady-state pressure distribution deviates significantly from adiabatic flow (Fig. 31).

An interesting example is the expansion flow around a sharp corner, known as Prandtl–Meyer expansion (PME), if the fluids start to condense within the centred expansion fan. The unique feature of such flows is the strong variation of the cooling rate $-dT/dt$ from infinite at the edge until zero in the far-field. With the assumption of steady flow, this problem has been investigated theoretically for subcritical as well as for supercritical heat addition by Delale and Crighton [40, 41]. The question is,
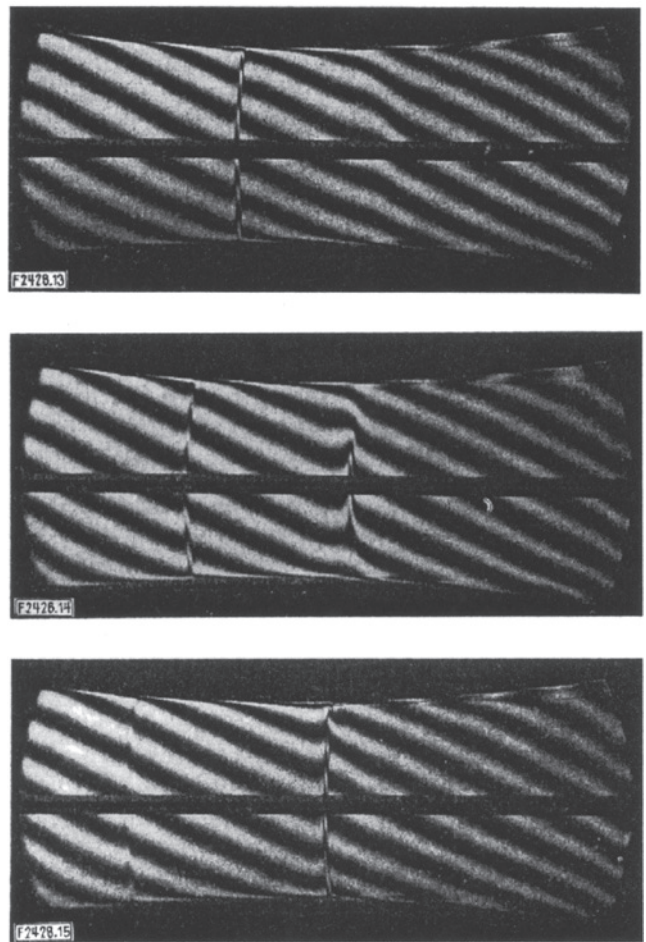

Fig. 29 Mach–Zehnder interferograms of one periodic cycle of self-excited oscillations of pure steam flow in nozzle No. 7 (see Table 1), flow from left, starting from top; frequency $f = 801$ Hz; Ludwieg tube, operating with water vapour, reservoir conditions: $T_{01} = 379.8$ K, $p_{01} = 1.16$ bar, original picture from Barschdorff [30]

what happens in such at one side infinitely unbounded flows, if the latent heat release increases more and more, supposed the onset remains in the regime $M > 1$. Experiments of Smith [42] and Frank [43] showed that oscillatory instabilities form, similar to those known from Laval nozzle flows. However, in these experiments the flow was bounded by solid walls from both sides, the lower wall formed the sharp corner and the upper was a plane wall. In principle, this configuration forms a half nozzle with a centred expansion at the throat. So far, it is quite understandable what was observed. Within a theoretically unbounded PME, where iso-lines of temperature, pressure, etc. coincide with the characteristics emerging from the edge, all disturbances caused by the local heat addition inside the fan evolve along iso-therms and tend to interact with the condensation onset from the very
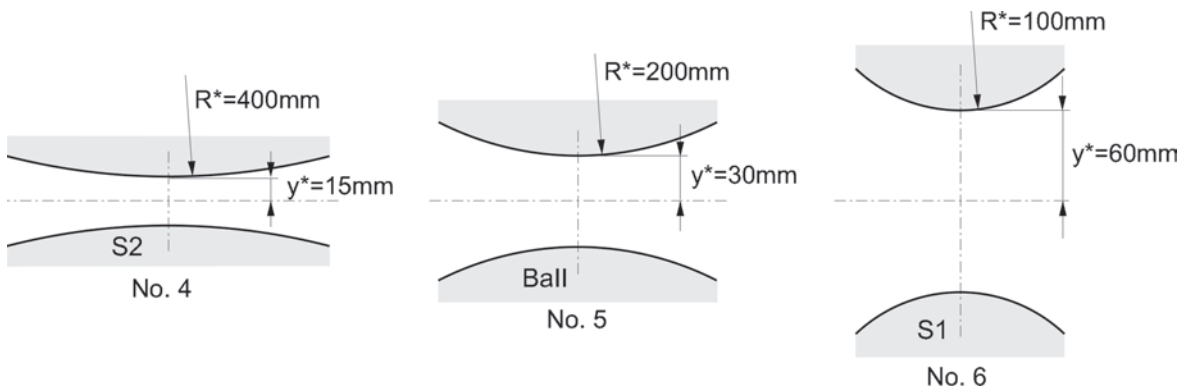
Fig. 30 Sketch of two-dimensional plane circular arc nozzles No. 4, 5, and 6 – from left, with identical cooling rates $(-\mathrm{d}T/\mathrm{d}t)^*_{\text{one-dimensional 293 K}} = 0.23$ K/μs

beginning. This is the classical configuration of a sonic heating front. If the unbounded PME with respect to condensation dynamics is considered, interpretation of this flow becomes even more complex. Because of the diminishing cooling rate at great distance from the edge, the flow remains fully frozen

at the edge and starts homogeneously nucleating close to the edge. At some greater distance heterogeneous effects become important, finally dominant and in the far-field condensation establishes in equilibrium. Simultaneously, the onset of condensation shifts towards saturation that usually locates in subsonic flow and the PME model is no more valid. This emphasizes the interesting nature of this special diabatic flow type, but interpretation of such flows requires careful considerations.
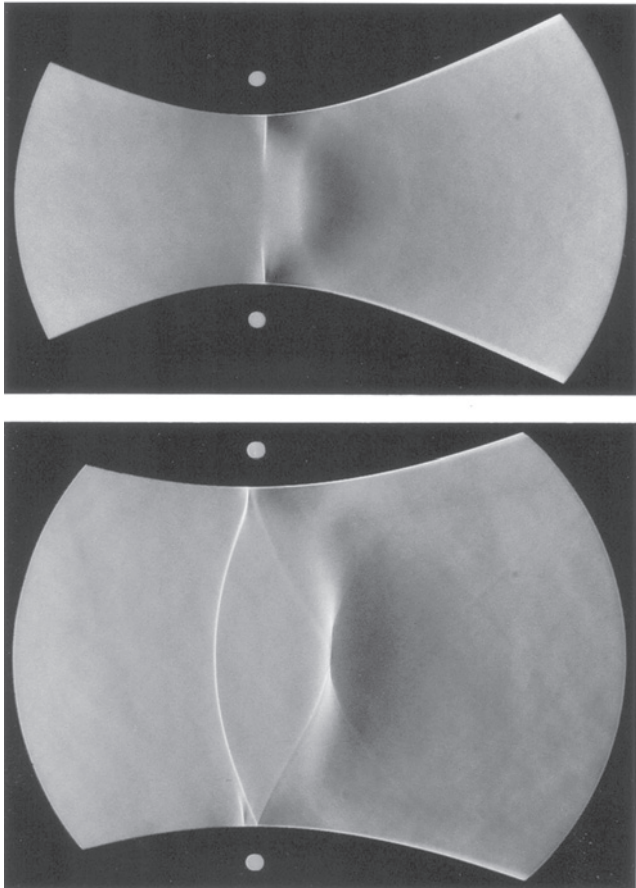
3.3.1.3 Stabilization by seeding. In flows of large-scale units such as steam turbines, pure homogeneous nucleation would be rather unlikely. The supply conditions of the working fluid, corrosion inside the system, etc. pollute the vapour with impurities that act as heterogeneous nuclei. During the expansion flow, both processes, homogeneous nucleation with droplet growth and wetting of the heterogeneous particles, interact with each other and the winner dominates the condensation process and all macroscopic gas dynamic effects. The following example shows how the increasing number concentration of seeding particles first weakly reduces the oscillation frequency. Finally, the oscillation disappears completely and the flow returns to steady state. The main mechanism is the reduction of the free energy, necessary for formation of nuclei, in the presence of solid particles. This shifts the onset of heat addition upstream, towards the saturation state and into the subsonic flow region. The characteristic diabatic compression ramp smears out and allows the flow to remain in steady state. The two-dimensional plane nozzle under consideration is depicted in Fig. 32 and the Schieren-type simulation (Fig. 33) shows how the frequency reduces in case of increasing particle concentration. Figure 34 makes clear that there exists typically a wide range of particle concentrations which is more or less ineffective and without remarkable effect on the dominant
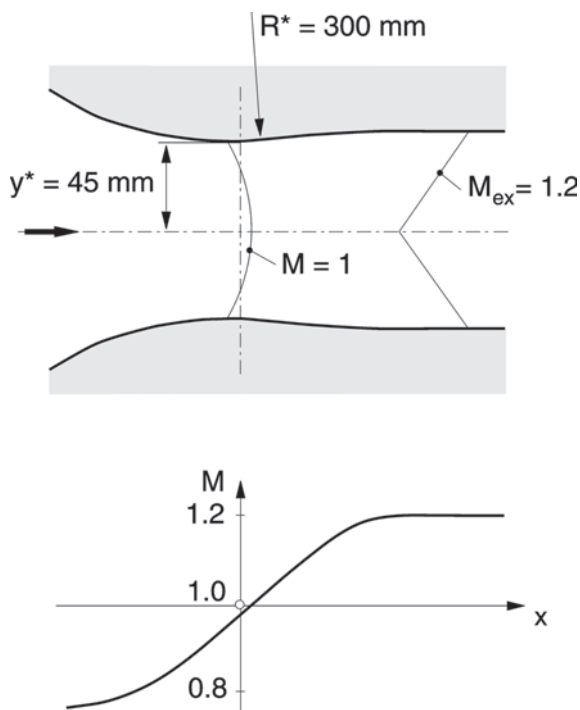

Fig. 31 Instantaneous pictures of local formation of unsteady shocks in strongly curved Laval nozzles, flow from left; top – nozzle No. 2, bottom – nozzle No. 3 (see Table 1)

Fig. 32 Sketch of two-dimensional plane parallel jet nozzle A1 (see Table 1), shape and isentropic Mach number distribution at the axis

homogeneous dynamics. However, in a narrow range seeding becomes effective. Because artificial seeding is appropriate to avoid additional non-equilibrium losses in steam turbines, knowledge of this most effective parameter range is an important precondition.

3.3.2 Unsymmetric instabilities

3.3.2.1 Bifurcation and moving oblique shock waves. Symmetric two-dimensional plane nozzle. The characteristic feature of expanding flows in circular arc nozzles for non-equilibrium phase transition is the approximately constant cooling rate $-\mathrm{d}T/\mathrm{d}t$ (K/μs) in the relevant transonic flow region near the throat. Therefore, for good approximation to characterize the time-scale of such plane circular arc nozzles the critical value at sonic conditions is taken $(-\mathrm{d}T/\mathrm{d}t)^*$. The constancy of this important parameter, i.e. the linear variation of all important thermodynamic variables such as temperature and static pressure simplifies the problem essentially. But if during the expansion and non-equilibrium condensation process, the time-scale varies locally, understanding and interpretation of the dynamics of this two-phase flow is more sophisticated.

As an example, the nozzle already shown in Fig. 32 is investigated where the cooling rate at the throat $-(\mathrm{d}T/\mathrm{d}t)^* = 0.15$ K/μs diminishes to zero at the exit, i.e. with parallel outflow and constant isentropic exit Mach number, here $M_e = 1.2$. From section 2.2, it is clear that the absence of area variation increases the flow sensitivity against diabatic disturbances. Therefore, this nozzle type is well appropriate for studying instabilities caused by latent heat release in condensing flows. At the beginning and for moderate values of ϕ_0, the known symmetric shock motion of mode 1 is observed (Fig. 35, left).

In the range of approximately 45 per cent $< \phi_0 <$ 75 per cent, the frequency increases approximately linearly from 200 Hz to 400 Hz (Fig. 36). At $\phi_0 = 75$ per cent, dynamics and flow pattern change completely. The frequency increases suddenly to more than 800 Hz and oblique moving shock systems form and move monotonically opposite to the oncoming flow (Fig. 35, right).

This phenomenon was first detected in experiments by Adam and Schnerr [26] and is perfectly confirmed by numerical simulation using the Euler equations. Careful numerical investigations confirm that this new instability in the unsteady flow region and the bifurcation are not controlled by viscous effects. It is definitely an inviscid instability and represents an interesting example for bifurcation of the Euler equations in the unsteady transonic flow regime. Theoretical solutions by Simpson and White [44] predict similar bifurcations in pure steam flow.

The sudden increase of frequency and static pressure disturbance are of immediate practical interest. Moreover, this very unusual dynamical behaviour of shock waves in homogeneously condensing flows is of fundamental interest for investigations of dynamical systems in fluid mechanics and gives some insight into the topology of instabilities of generalized reacting transonic flows.

Transient rearrangement from symmetric to unsymmetric flow instability. The transient behaviour of symmetric oscillations above a certain threshold value of the vapour content is well confirmed by the following experiment for registration of the time-dependent formation of this instability just after starting the flow in the intermittent indraft wind tunnel (Fig. 37). At the beginning, one observes a symmetric oscillation, which seems to be stable for a limited number of periods, before transition to the unsymmetric mode takes place. Five sequences of a high-speed movie show the rearrangement of the flow field from symmetric to the unsymmetric mode.

At left the symmetric oscillation is already weakly disturbed, at the right side the unsymmetric mode is fully developed. Overall, the transition takes about 60 periods. Figure 38 confirms the
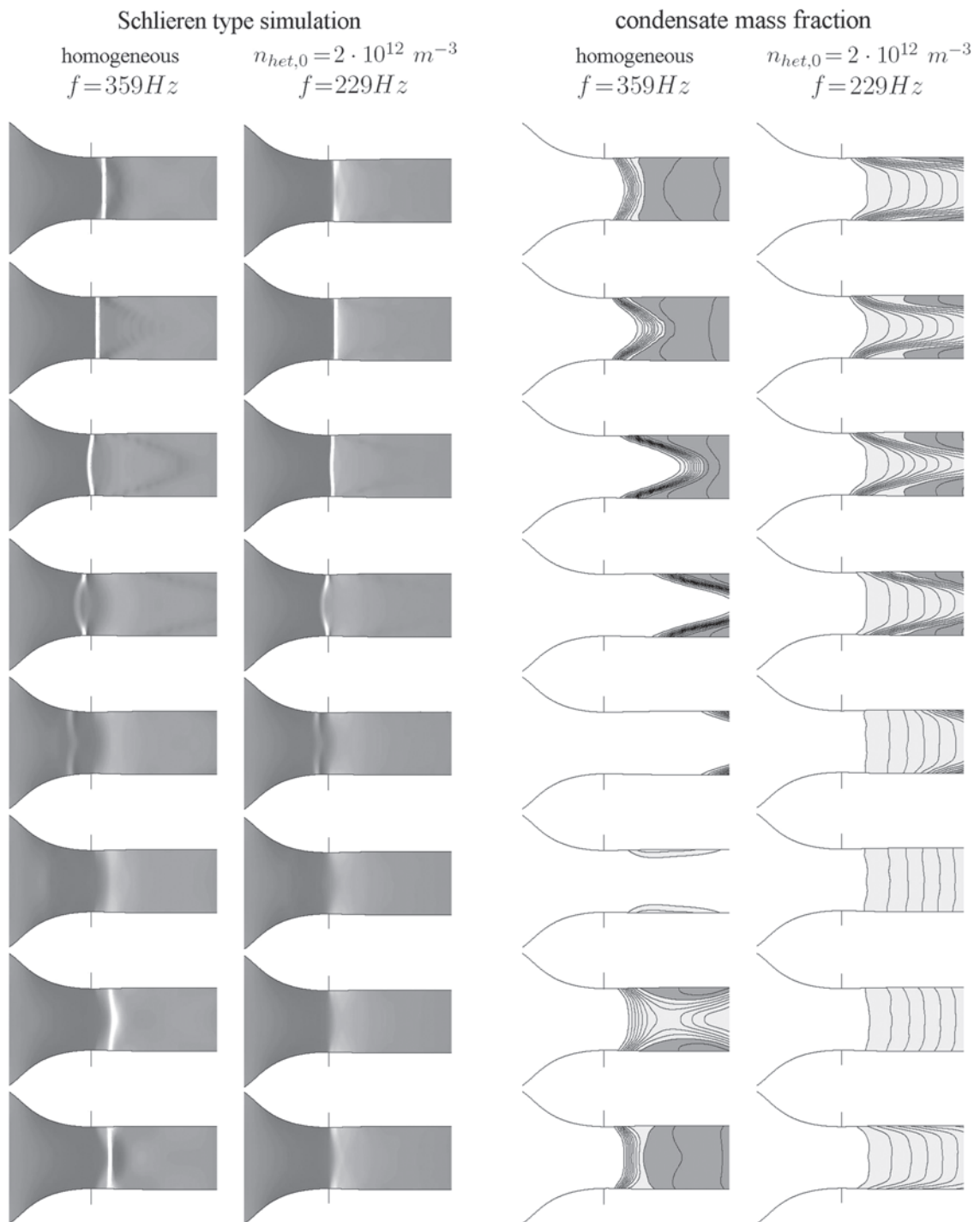
Schlieren type simulation

homogeneous	$n_{het,0} = 2 \cdot 10^{12}\ m^{-3}$
$f = 359 Hz$	$f = 229 Hz$

condensate mass fraction

homogeneous	$n_{het,0} = 2 \cdot 10^{12}\ m^{-3}$
$f = 359 Hz$	$f = 229 Hz$

Fig. 33 Comparison of symmetric oscillations of homogeneously and mixed homogeneously/ heterogeneously nucleating unsteady flow in parallel jet nozzle A1; humid air, reservoir conditions: $T_{01} = 295.0$ K, $p_{01} = 1.0$ bar, $\phi_0 = 65.0$ per cent; spherical seeding particles: $r_{p,\ het} = 10^{-8}$ m, contact angle $30°$. Grey scale of condensate mass fraction: light-grey – $g/g_{max} > 0.05$, dark-grey – $g/g_{max} > 0.5$, increment 0.05, numerical simulation

experimental observation by superimposing the calculated transient static pressure signals at the nozzle throat at the upper and lower wall. Again, after initialization, it observed perfect symmetric behaviour with identical signals at the top and bottom wall,

respectively, and after a short transient state the fully developed unsymmetric mode with doubling of the frequency. The logarithmic pressure difference between the upper and lower nozzle wall shows the characteristic linear growth of disturbances.
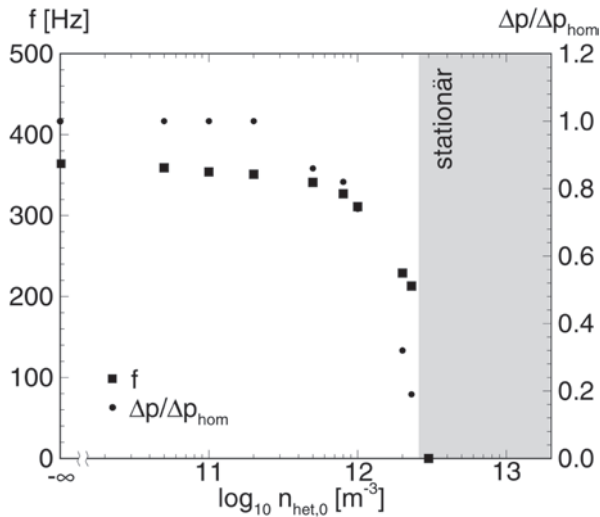
Fig. 34 Frequency f of the symmetric oscillation and dimensionless static pressure amplitude dependent on the seeding particle concentration $n_{het,0}$ at the reservoir, numerical simulation (for data, see Fig. 33)
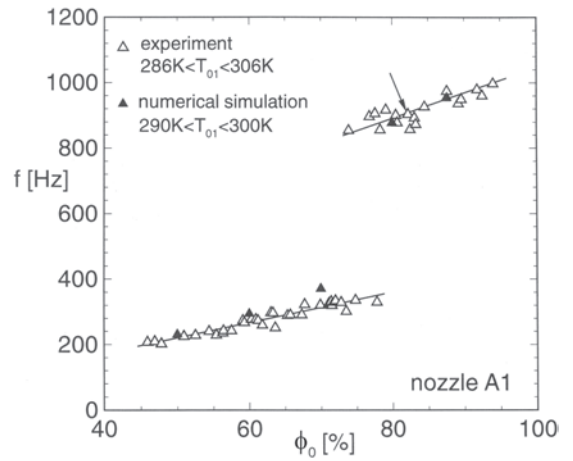

Fig. 36 Frequency dependence on the relative humidity in the reservoir ϕ_0 in nozzle A1; experimental results compared with numerical simulations. Lower branch: $287.5\,\text{K} \leqslant T_{01} \leqslant 305.0\,\text{K}$, numerical simulation $T_{01} = 300.0\,\text{K}$; upper branch: $285.5\,\text{K} \leqslant T_{01} \leqslant 295\,\text{K}$, numerical simulation $T_{01} = 285.0$ and $295.0\,\text{K}$

Because of the many simplifications of the classical steady-state capillary nucleation theory and the averaging droplet growth models used here, it is quite interesting and important to note that an inviscid CFD simulation tool based on this phase transition model is accurate not only in reproduction of the periodic unsteady regime, but also for
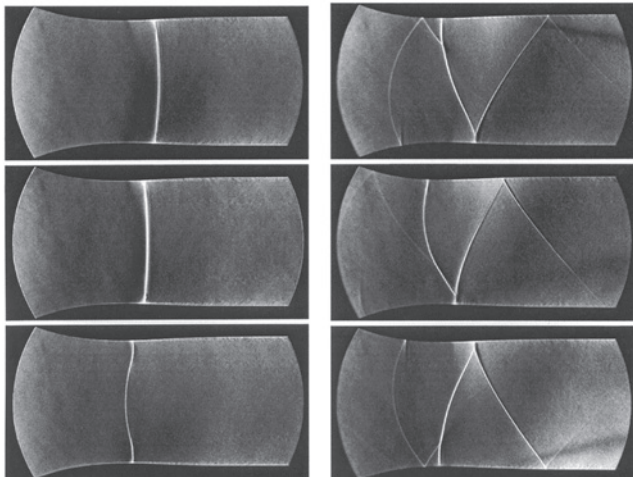

Fig. 35 Experiment – bifurcation in nozzle A1, Schlieren pictures of symmetric and unsymmetric flow oscillation: symmetric mode – left, $f = 225$ Hz, $T_{01} = 292.8$ K, $p_{01} = 1.0$ bar, $\phi_0 = 51.6$ per cent, $x = 7.4\,\text{g}_{H_2O}/\text{kg}_{dry\ air}$; unsymmetric mode – right,, $f = 905$ Hz, $T_{01} = 288.2$ K, $p_{01} = 1.0$ bar, $\phi_0 = 82.0$ per cent, $x = 8.8\,\text{g}_{H_2O}/\text{kg}_{dry\ air}$
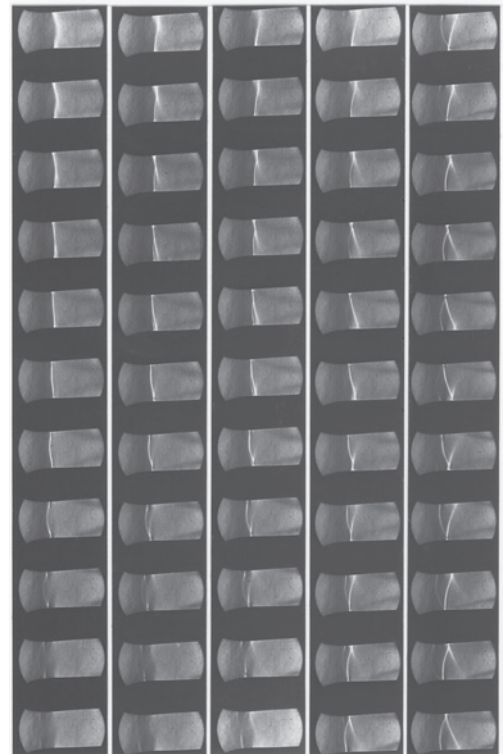

Fig. 37 Experiment – transient rearrangement from symmetric to unsymmetric flow oscillation in nozzle A1, high-speed movie with 7000 pps, time increases from top left; reservoir conditions: $T_{01} = 290.6$ K, $p_{01} = 1$ bar, $\phi_0 = 77.1$ per cent, $x = 9.8\,\text{g}_{H_2O}/\text{kg}_{dry\ air}$; frequency $f = 333$ Hz – fully developed symmetric oscillation and $f = 897$ Hz – fully developed unsymmetric oscillation
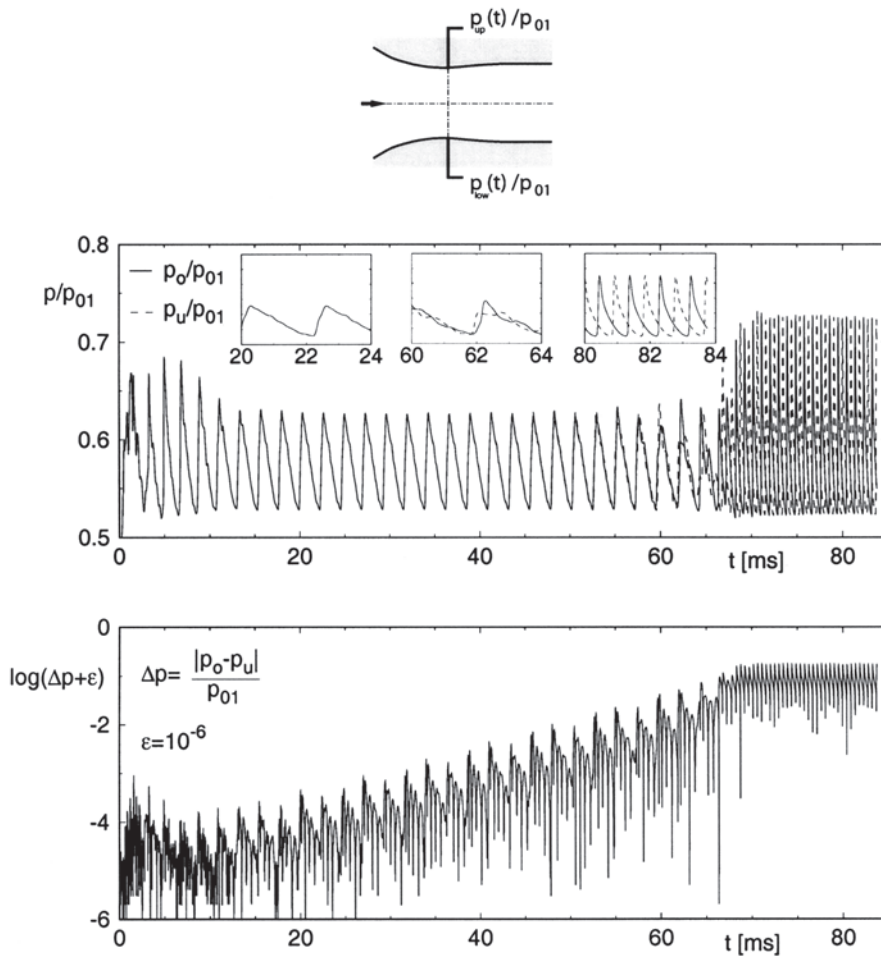
Fig. 38 Transient rearrangement from symmetric to unsymmetric flow oscillations – exponential growth of static pressure disturbance in unstable symmetric flow oscillations, numerical simulation

investigation of the transient rearrangement between different types of instabilities.

Unsymmetric two-dimensional plane nozzle. Interpretation of unsymmetric flow instabilities observed in experiments requires careful consideration of the real situation. The formation of unsymmetric flow pattern may be caused by imperfect manufacturing or insertion of the nozzle, by non-homogeneous inflow conditions, instantaneous disturbances, etc. Similar arguments hold for the CFD simulation including details of the algorithm and discretization technique. All these reasonable arguments could be refuted be performing the following test using the two-dimensional plane nozzle A1A having a priori a strong asymmetric design (Fig. 39). As before, the fluid is humid air and the simulation neglects viscosity.

Despite the strong unsymmetric nozzle shape, the Schlieren-type CFD simulation (Figs 40 and 41) reveals for identical inflow conditions two completely different flow topologies with the characteristic

difference between the symmetric and the unsymmetric oscillations [45]. The frequency increase is not as much as in perfect symmetric nozzles, but the simultaneous existence of two separate
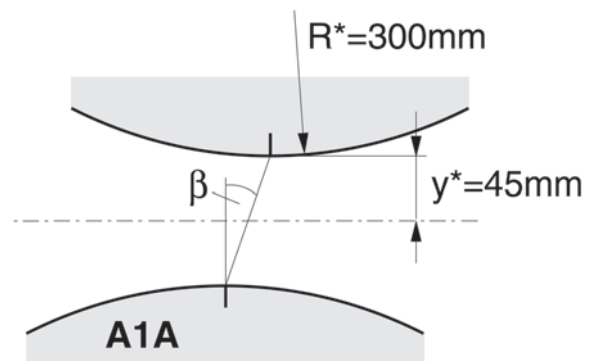

Fig. 39 Sketch of shifted two-dimensional plane circular arc nozzle A1A, shift angle $\beta = 40°$
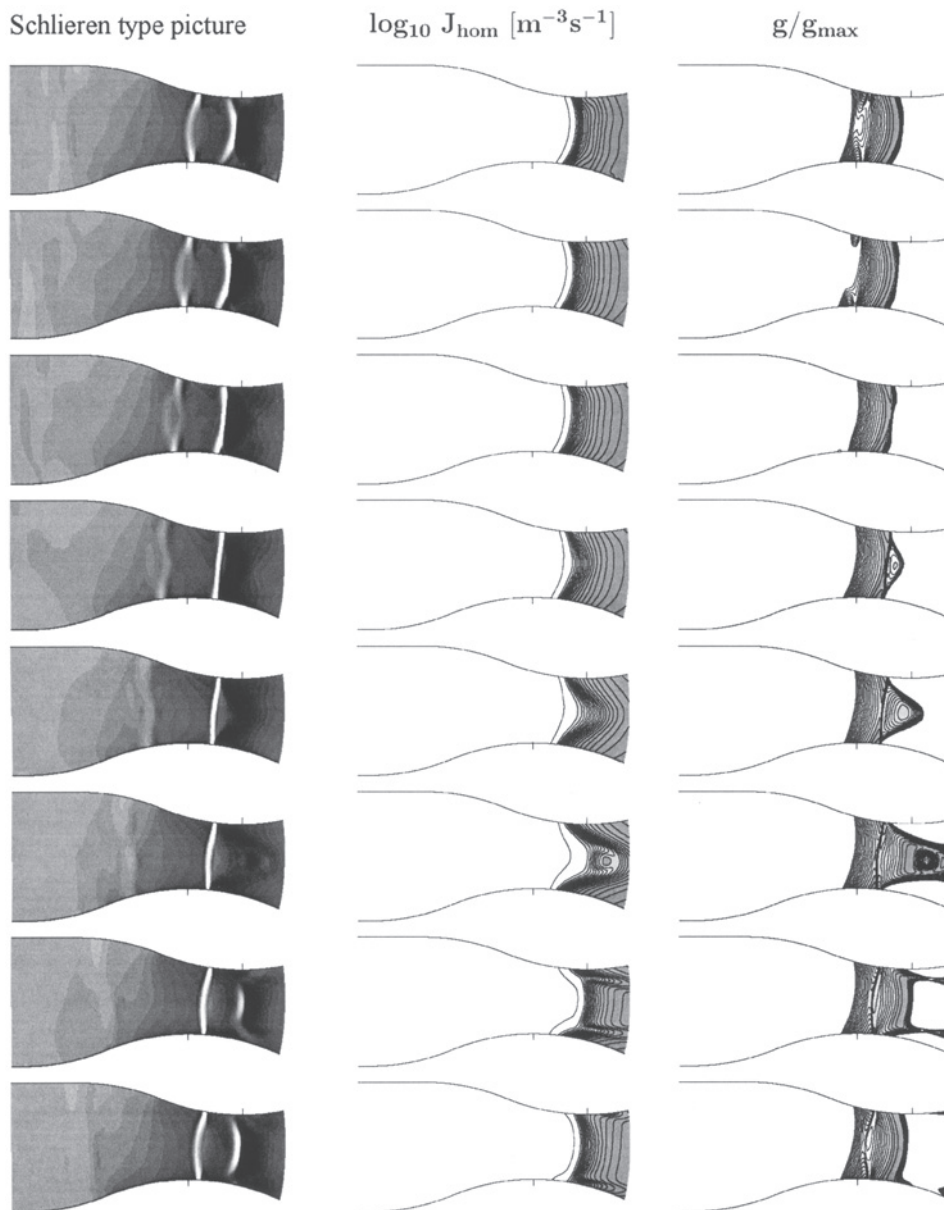
Fig. 40 One period of quasi-symmetric oscillation in the shifted nozzle A1A, flow from left, frequency $f = 854$ Hz; reservoir conditions: $T_{01} = 295.0$ K, $p_{01} = 1.0$ bar, $\phi_0 = 90.0$ per cent, inviscid numerical simulation

instabilities under such conditions confirms that the observed bifurcation mechanism is generally valid and establishes independent of reasonable imperfect operating conditions.

Axisymmetric nozzle. The geometry of the axisymmetric nozzle under consideration is obtained by using a nozzle of circular cross-section with the same diameter as the width shown in Fig. 32. Because of the higher cooling rate in three-dimensions, the limit of stability is shifted to $\phi_0 = 60–65$ per cent. Then the flow becomes unsteady and starts with symmetric oscillations. At $\phi_0 = 87.5–90$ per cent relative humidity, the unsteady flow reaches

the lower branch of the hysteresis where the system has more than one solution. In this axisymmetric nozzle, the higher-order instability mechanism enables the diabatic shock surface to spiral around the centerline. The frequency increases from 942 to 1350 Hz [46] (Figs 42–44).

3.4 Unsteady condensing flow through axial cascades

This section explains steam flows operating under conditions typical for LP turbines. First of all, it is
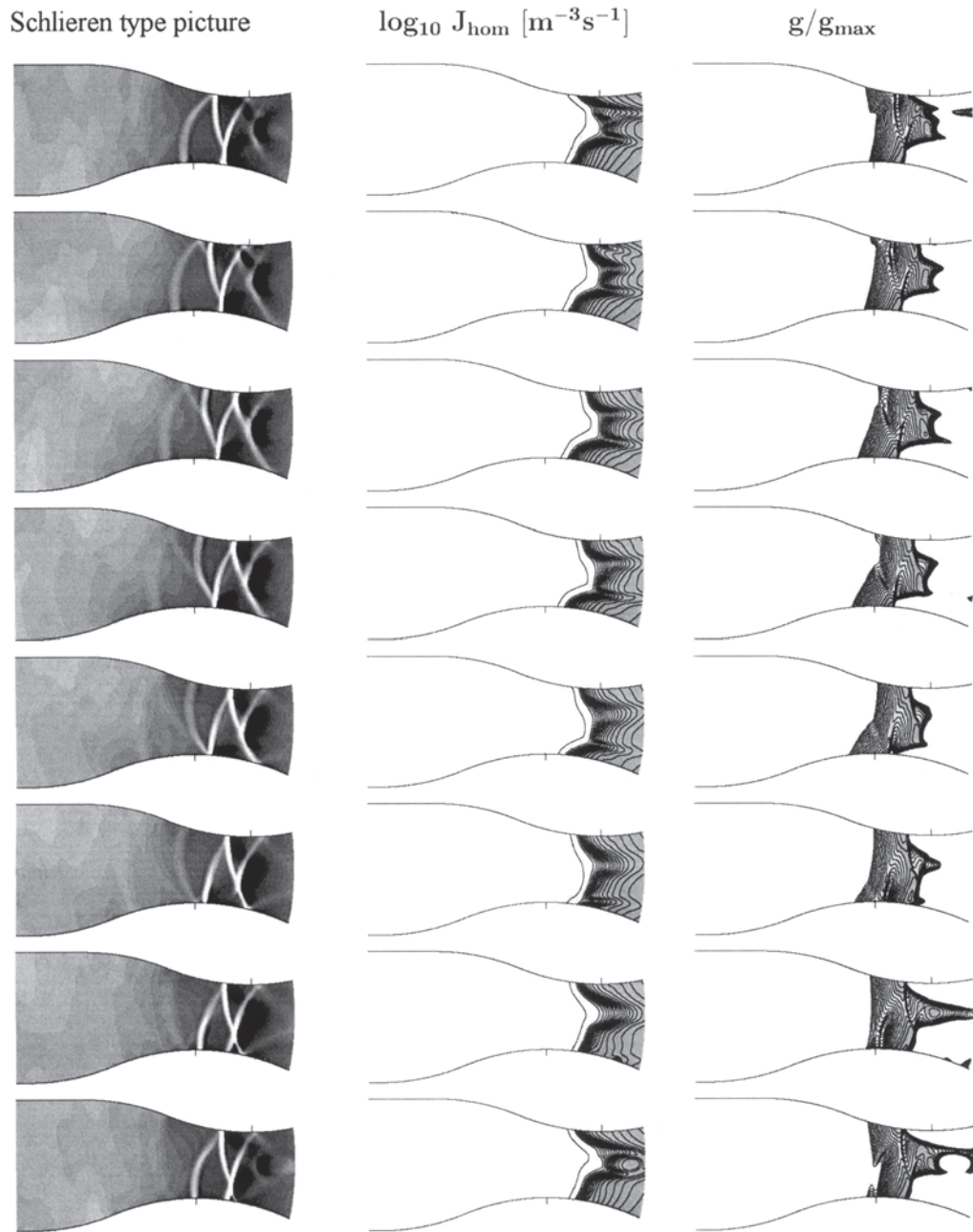
Schlieren type picture $\log_{10} J_{\mathrm{hom}}$ [m^{-3}s^{-1}]   g/g$_{\mathrm{max}}$

Fig. 41   One period of unsymmetric oscillation in the shifted nozzle A1A, flow from left, frequency $f = 1082$ Hz; reservoir conditions: $T_{01} = 295.0$ K, $p_{01} = 1.0$ bar, $\phi_0 = 90.0$ per cent, inviscid numerical simulation

important to note and to understand that self-excitation as seen in nozzle flow is rather unlikely to appear in axial cascades. The main reason is that the flow through axial cascades does not experience a comparable constrain due to solid walls between inlet and exit planes, as in a Laval nozzle. It is already seen in section 2.2 that the area constrain is one of the necessary conditions for the formation of instabilities. So, thermal choking with unsteady moving shocks is rather unlikely to appear. In blade-to-

blade flow of axial cascades, due to the stagger angle, the sonic throat and the important transonic/slightly supersonic regime with substantial latent heat release are usually confined by the suction side of one blade and the wake of the neighbouring blade, i.e. by a free boundary. Therefore, in case of latent heat release with equivalent displacement effects in this region, the free boundary adjusts the flow automatically so as to remain in steady state. This self-adaptation avoids thermal chocking with
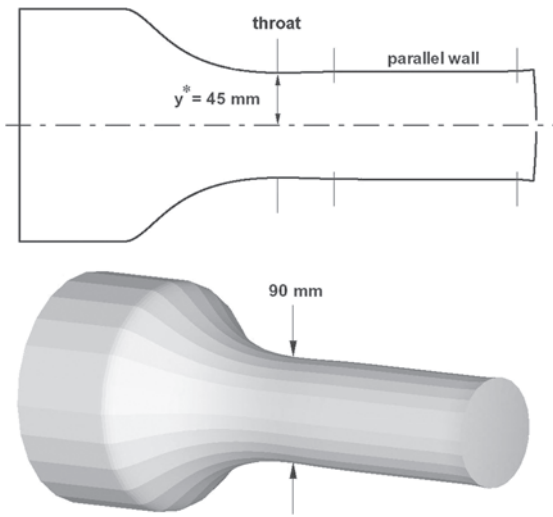
Fig. 42 Shape and data of three-dimensional axisymmetric nozzle A1 3D (see Table 1)

unsteadiness, but it turns the flow angle β_2 at the trailing edge of the blade so that momentum and efficiency decrease.

However, self-excitation of condensing axial cascade flow is to be expected if the stagger angle is artificially reduced, so that the flow regime with latent heat release, i.e. the area of maximum nucleation rate and droplet growth, is confined by solid walls at both sides, the suction side and pressure side of neighbouring blades.

Nevertheless, because of high-frequency blade wake oscillations and periodic waves caused by rotor/stator exchange, there are other excitation mechanisms interacting with the sensitive transonic condensing vapour flow, which will be explained in the following.

Because of the great scientific potential and the economical relevance of these complex unsteady transonic two-phase flows, this problem is subject
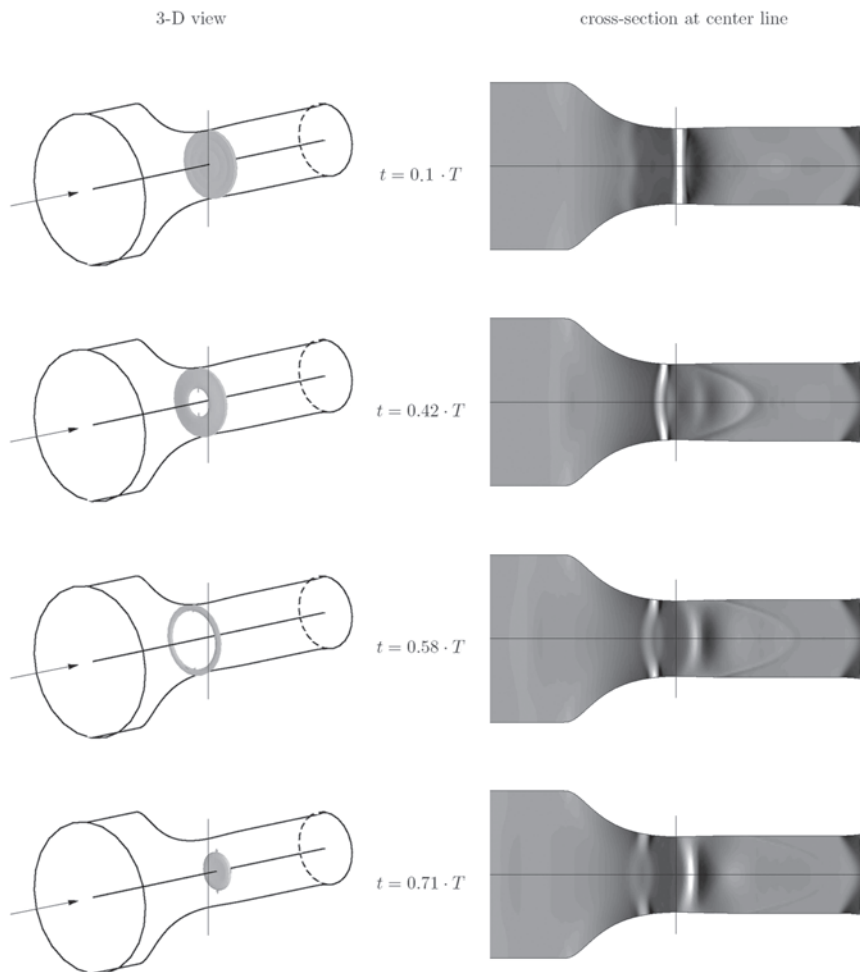

Fig. 43 Symmetric oscillation in three-dimensional axisymmetric nozzle A1, flow from left, frequency $f = 942$ Hz; reservoir conditions: $T_{01} = 295.0$ K, $p_{01} = 1.0$ bar, $\phi_0 = 95.0$ per cent, inviscid numerical simulation

3-D view   cross-section at center line

$t = 0.1 \cdot T$

$t = 0.29 \cdot T$

$t = 0.57 \cdot T$
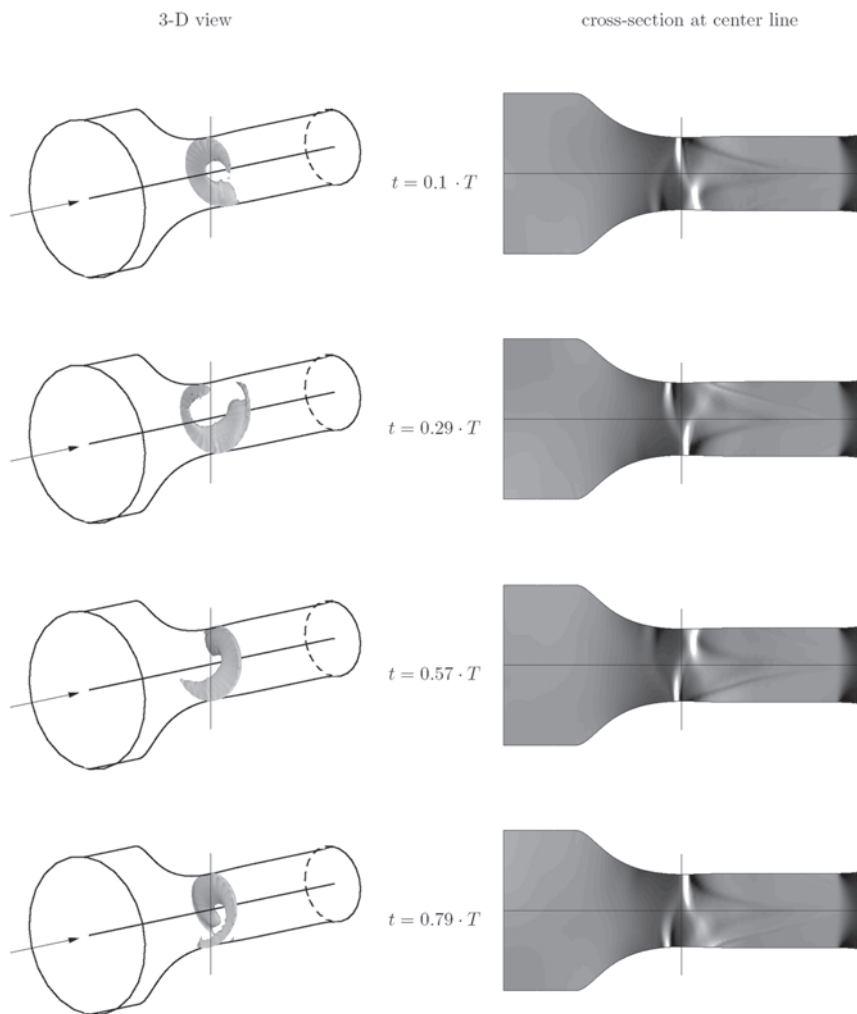
$t = 0.79 \cdot T$

Fig. 44 Unsymmetric oscillation with spiraling shock surface in three-dimensional axisymmetric nozzle A1, flow from left, frequency $f = 1350$ Hz; reservoir conditions: $T_{01} = 295.0$ K, $p_{01} = 1.0$ bar, $\phi_0 = 95.0$ per cent, inviscid numerical simulation

of many important theoretical, numerical, and experimental investigations (see, e.g. [47–52]).

The first mechanism under condensation is driven by the shedding of shear layers at blade trailing edges, whereas the second type concerns the convection of wakes with distinct high dissipative losses and therefore higher temperature fluctuations from the stator into the rotating frame of reference of the rotor. Both mechanisms are clearly driven by the fluid viscosity.

3.4.1 Wake interactions

3.4.1.1 Periodic nucleation in wake flow. The first example concerns the high-frequency vortex shedding from the blunt trailing edges of the rotor. The origin of the related periodic excitation locates within the nucleating transonic flow regime at the

blade trailing edges. This source initiates high-frequency pressure and temperature fluctuations that interfere with the nucleation process in the entire cross-section from blade to blade and trigger the time-dependent droplet size distribution behind the cascade. The related unsteady phenomenon is known as wake chopping (see, for instance, the investigation of Bakhtar and Heaton [53]). Figure 45 shows numerical results of the turbulent flow simulation through a VKI 1 rotor, the steam is assumed to condense homogeneously, heterogeneous effects are excluded. All relevant data are given in the figure caption. The vortex shedding frequency at the blunt trailing edge is $f_{vs} = 22.55$ kHz with the Strouhal number $St = 0.22$. In adiabatic flow the shedding frequency is lower, about 17 kHz. The time-dependent variation of the nucleation process at the trailing edge correlates with the unsteady

$t = 1/3 \cdot T$ $t = 2/3 \cdot T$ $t = T$

M_f

J_{hom}

g

$\bar{r}$

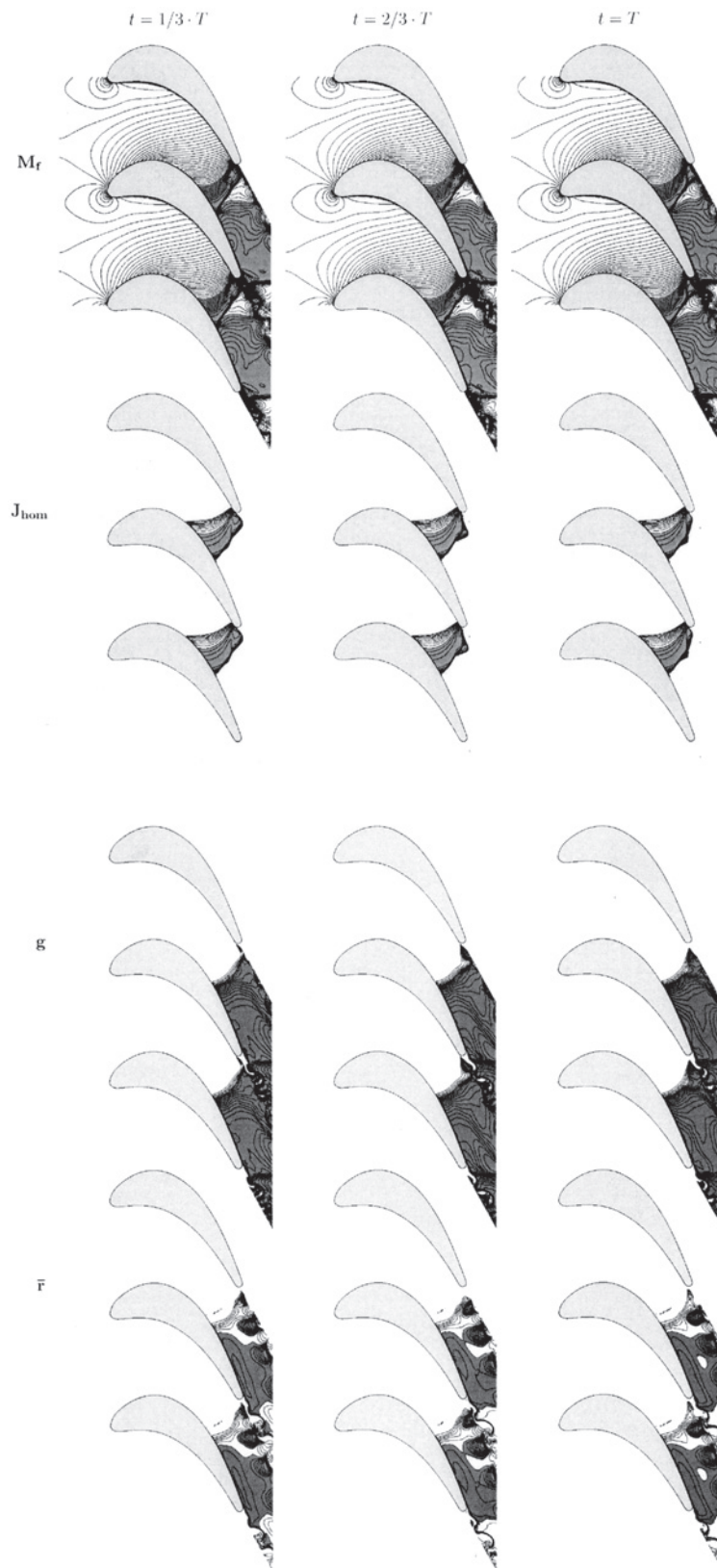**Fig. 45** Vortex shedding from trailing edge of VKI-1 turbine cascade, homogeneously condensing turbulent flow of pure steam; flow data: $T_{01} = 357.5$ K, $p_{01} = 0.417$ bar, $\beta_1 = 120°$, $p_2 = 0.194$ bar, $Re_2 = 1.13 \times 10^6$; vortex shedding frequency $f_{vs} = 22.5$ kHz, Strouhal number, $St = 0.22$; frozen Mach number, nucleation rate, wetness fraction and mean droplet radius, numerical simulation
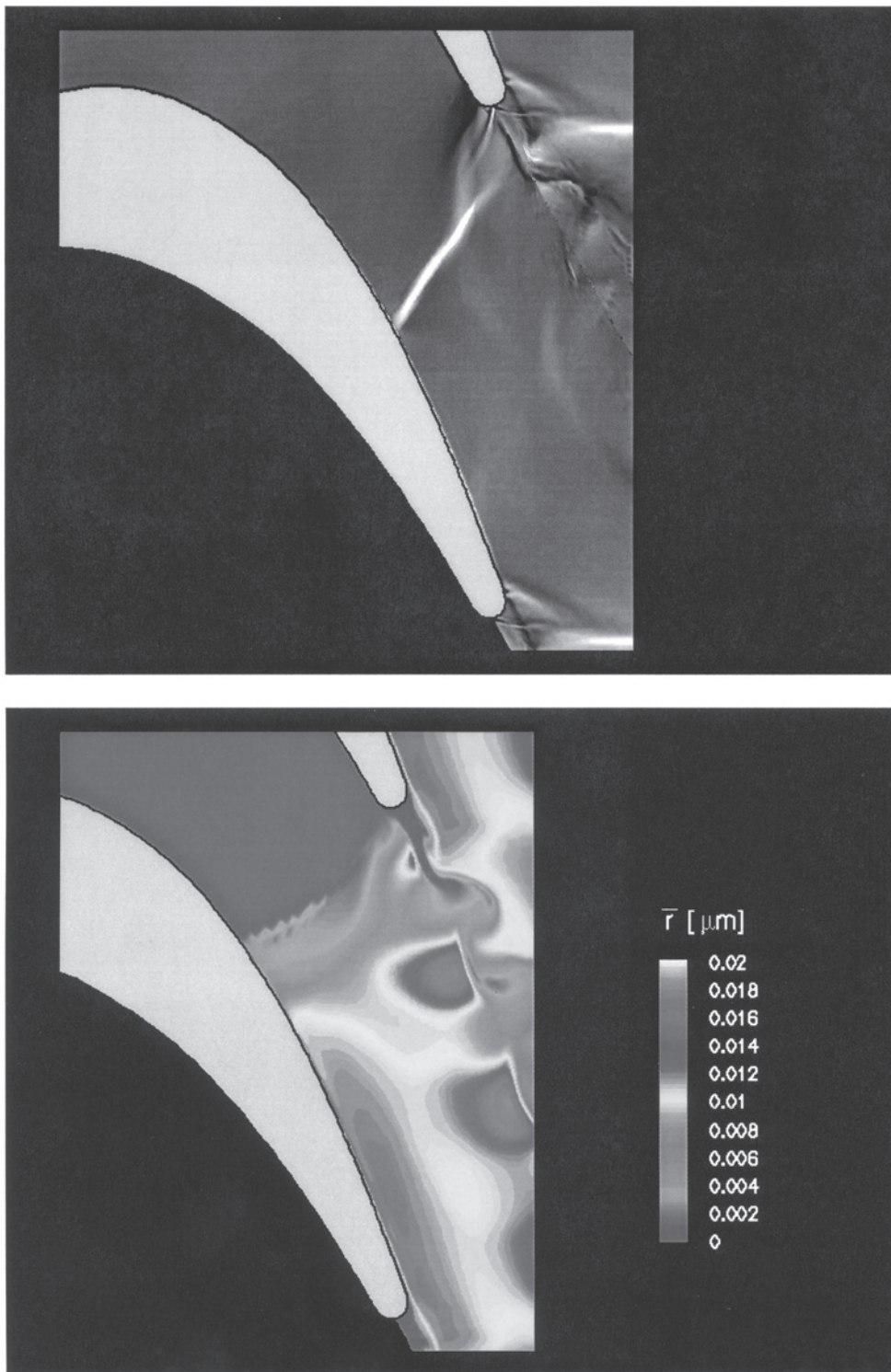
Fig. 46 Close up of Fig. 45, comparison of Schlieren-type visualization and unsteady droplet size formation triggered by the wake

local expansion around the blunt edge and the unsteady variation of intensity and position of the oblique shock system emerging from the edge. The strongest effects develop directly at the edge, here the homogeneous nucleation rate varies about two orders between $J = 10^{25}$ and 10^{27} m^{-3} s^{-1}. Figure 46 is an instantaneous Schlieren-type picture, together with the droplet size distribution $\bar{r}$ at this instant. This enlargement shows that the periodic wake oscillation behind the blade initiates a well-defined

chain of local spots with high supersaturation and high nuclei concentrations which are convected downstream. In principle, the wake acts like an unsteady moving elastic wavy wall in transonic supersaturated steam flow, and therefore the observation is quite understandable.

Figure 47 presents the resulting time-dependent variation of the wetness g, the droplet size $\bar{r}$, and the exit flow angle β_2 in the reference plane '2' 15 per cent of the blade chord ($c = 100$ mm) behind the cascade. The lateral extension corresponds to twice of the pitch ($p = 71$ mm). To emphasize the additional effects, caused by the unsteadiness, the results of the time-dependent simulation are compared with an artificial steady-state flow calculation. For steady flow simulations, the unsteady code version was modified to operate with reduced spatial and time-dependent

resolution, in principle by increasing artificial dissipation. For instance, outside the wakes the variation of the angle β_2 is of the order of $7°$, and in the same region Δg is about 0.006. Within the wakes the differences of the steady and unsteady flow model are more distinct. The maximum droplet size variation $\Delta\bar{r}$ locates close to the wake and is about 0.01 μm.

3.4.1.2 Separation-controlled frequency variation due to condensation. This section investigates the typical very slender axial rotor blades of the last stages of LP steam turbines, taking shape and operational data from Bakthar *et al.* [54]. Pitch and chord are equal and about 190 mm. Figure 48 compares single-phase flow results with those of homogeneously condensing flow. Pressure and temperature and all other conditions were kept
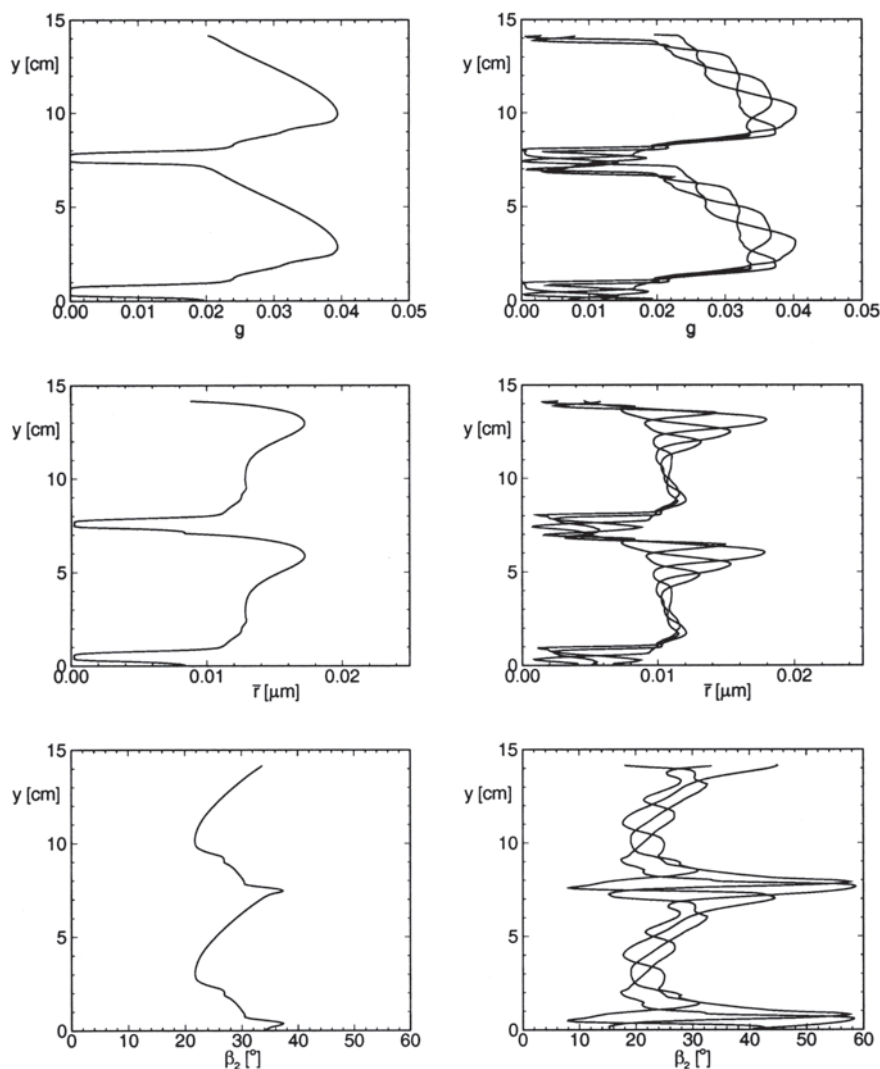
Fig. 47   Comparison of steady and unsteady flow through VKI-1 turbine cascade by wetness, mean droplet size, and flow angle at control plane '2' behind the blade row. For unsteady flow data and parameter, see Fig. 45
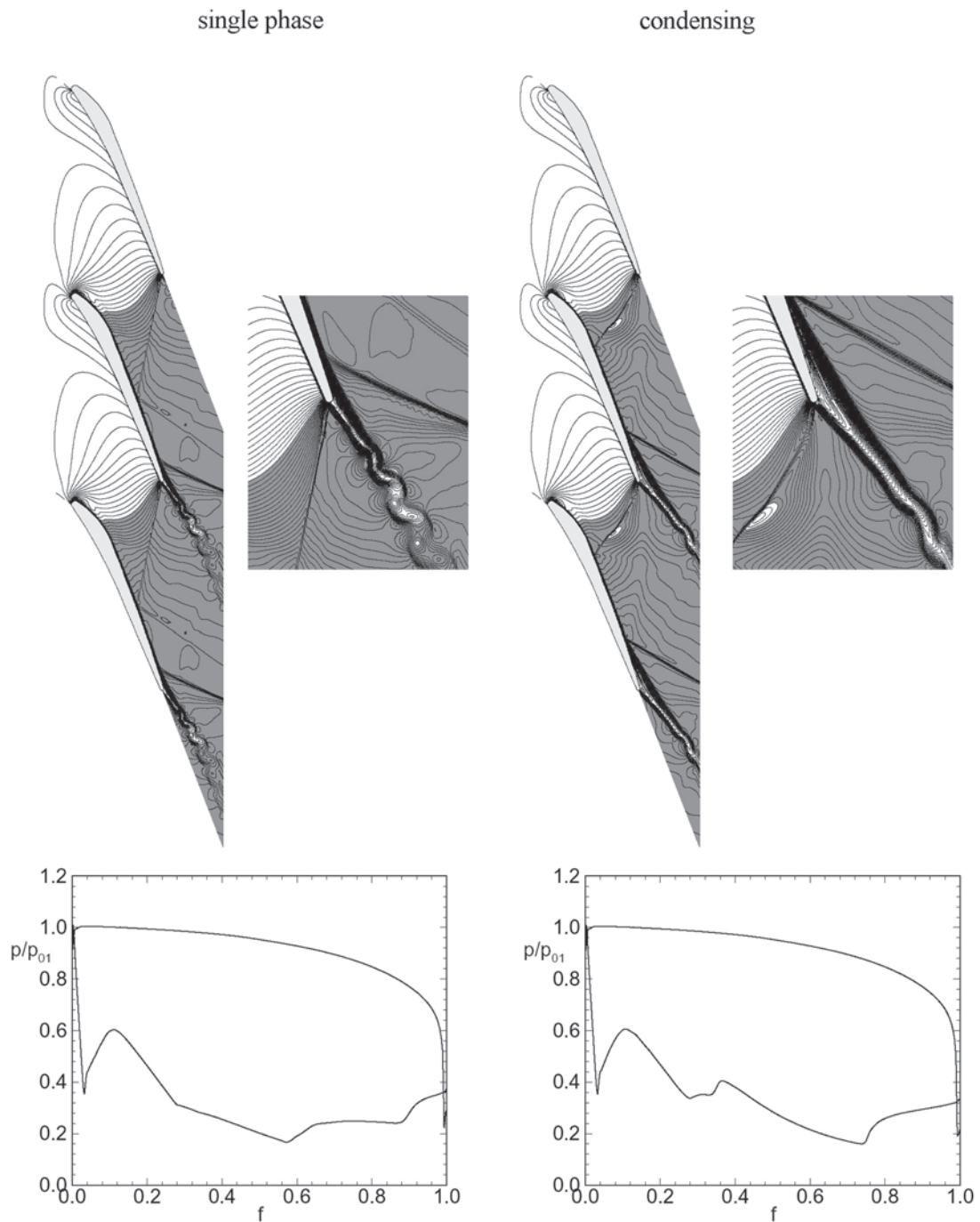
single phase   condensing

Fig. 48 Comparison of single-phase and homogeneously condensing turbulent steam flow through BAK-1 turbine cascade, flow data: $T_{01} = 354.0$ K, $p_{01} = 0.400$ bar, $\beta_1 = 52°$, $p_2 = 0.133$ bar, $M_{2, is} = 1.38$, $Re_2 = 1.15 \times 10^6$, f = arc length of blade numerical simulation

constant, except that in case of 'single-phase flow' the condensation model was de-activated. The significant difference is the oblique shock-induced separation due to condensation on the suction side of the blade. The shedding frequency decreases from 23 kHz in single-phase flow to 16.4 kHz with condensation (Fig. 49). Simultaneously, the separation point moves upstream and forms a thicker

separation zone. The time-dependent density signal at the monitor point in the reference plane behind the cascade emphasizes the reduction of the oscillation frequency. In the previous example, the shedding frequency was higher with condensation. The reason for the opposite trend here is the upward shift of the separation point, causing a thicker separation zone. Because the Strouhal
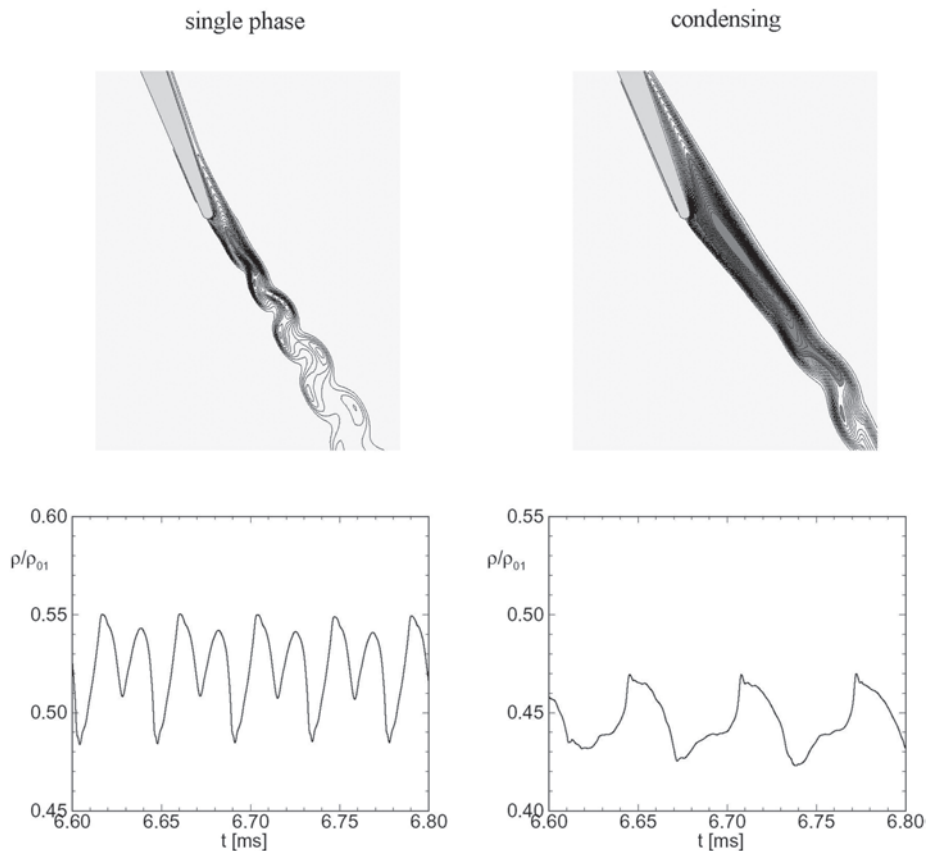
single phase   condensing

Fig. 49   Close up of Fig. 48 and comparison of vortex shedding frequency; single-phase flow frequency $f_{vs} = 23.0$ kHz, homogeneously condensing flow $f_{vs} = 16.4$ kHz, numerical simulation

number is approximately constant, about 0.2, the thicker separation zone correlates with the lower frequency.

3.4.2   Forced excitation by rotor/stator interaction

Figure 50 is a schematic sketch of the way in which the wakes from one blade row interact with, and are segmented, by the following rows. It is obvious that convective layers (dark shaded area) of higher dissipation and therefore with higher temperature become superposed with the averaged blade-to-blade flow. From the sensitivity of nucleation against small temperature fluctuations, it is clear that the assumption of uniform temperature and entropy at the inlet plane of turbine stages has to modified, to account for this unsteady wake effects.

3.4.2.1 Single blade row with unsteady inflow condition. This section continues with the same cascade geometry as already investigated in the previous section. Because a complete model for simulation of the continuous transition from the stator in the rotating frame of reference of the rotor requires
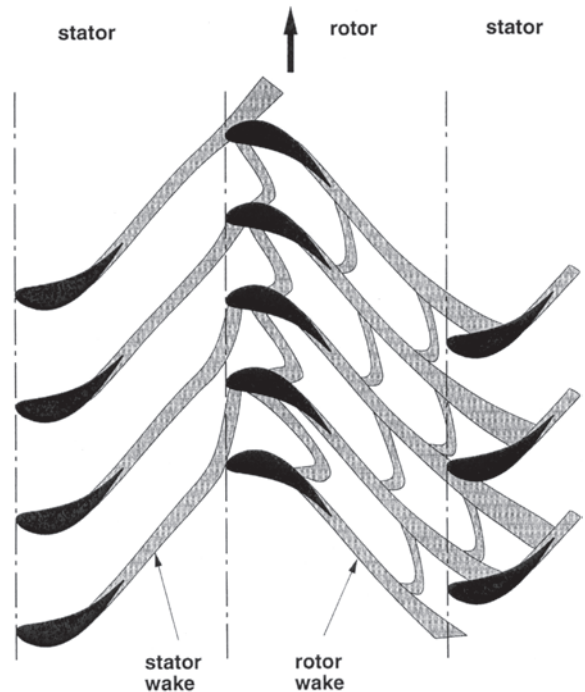

Fig. 50   Sketch of passage of blade wakes through successive blade rows

$t = 1/4 \cdot T$ $t = 1/2 \cdot T$ $t = 3/4 \cdot T$ $t = T$
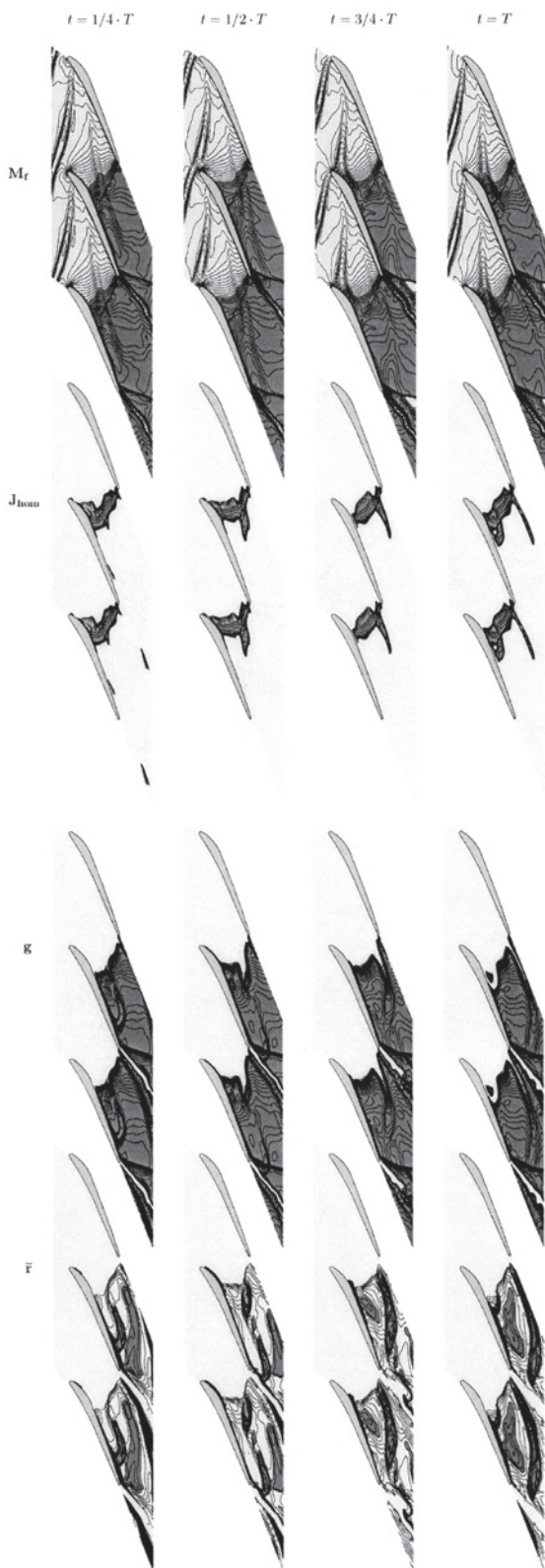
M_f

J_{hom}

g

$\bar{r}$

Fig. 51 Numerical simulation of interaction of wakes with homogeneously condensing turbulent blade to blade flow through BAK-1 turbine cascade; flow model: unsteady inflow condition according to Hodson [**55**, **56**] for (flow data, see Fig. 48)

additional complex CFD techniques such as sliding interfaces, especially without averaging of thermodynamic variable across the interface, this section starts with a rather simple empirical model. This replaces the steady-state inflow conditions ahead of the blade row by an unsteady moving distribution for velocity and temperature, the static pressure is assumed to be constant. The dispersion of velocity and temperature is modelled according to Hodson [**55**, **56**] (for details, see thesis of Heiler [**45**]). The Mach number distribution of Fig. 51 depicts waves entering the blade row as expected from the sketch above. Next, the nucleation process is considered. Close to the leading edge, the strong expansion around the tip of this slender blade causes a primary nucleation zone, followed by the main nucleation zone further downstream. As soon as the high-temperature wake interferes with the primary nucleation zone, it disappears instantaneously and completely, but it recovers again shortly after. The stator wake moves further downstream, rotates according to the gradients of the velocity field of the mean flow and interacts with the main nucleation zone emerging from the trailing edge of the upper blade.

The time-scale of this forced excitation is determined by the circumferential speed and the total number of blades, here $T = 0.38$ ms corresponding to $f = 2.6$ kHz. The plot of g and $\bar{r}$ in the control plane 15 per cent of the chord behind the blades shows strong excitation of the droplet size distribution (Fig. 52). Compared with the average droplet radius $\bar{r} = 0.02$ μm, the maximum instantaneous value increases three times up to 0.06 μm. Finally, such stator wakes interact with boundary layers and shear layers and excite turbulence production (not shown here), especially in the wakes separating from the rotor blade trailing edges.

3.4.2.2 Sliding interface.   The complete stage under consideration consists of the VKI 1 rotor, already investigated in section 3.4.1.1 and a stator blade row of the same geometry. The advantage using this well-known blade type is the distinct blunt trailing edge that allows detailed investigation of vortex shedding from the stator (Fig. 53). Coupling of the rotating frame of reference with the non-rotating one is now realized by introduction of a sliding interface, here without reduction of the local order of the discretization [**57**]. Usually averaging of variables at interfaces is applied. But in case that nucleation and droplet growth begin already in the stator, careful treatment of all gradients at the interface is necessary for preservation of the existing microscale liquid phase during convection through the interface and towards the rotor. Averaging of thermodynamic variables would result in unrealistic smearing of important condensation details. The quality of the present technique is observable in Fig. 54, for instance, by the Schlieren-type visualizations. Figure 54
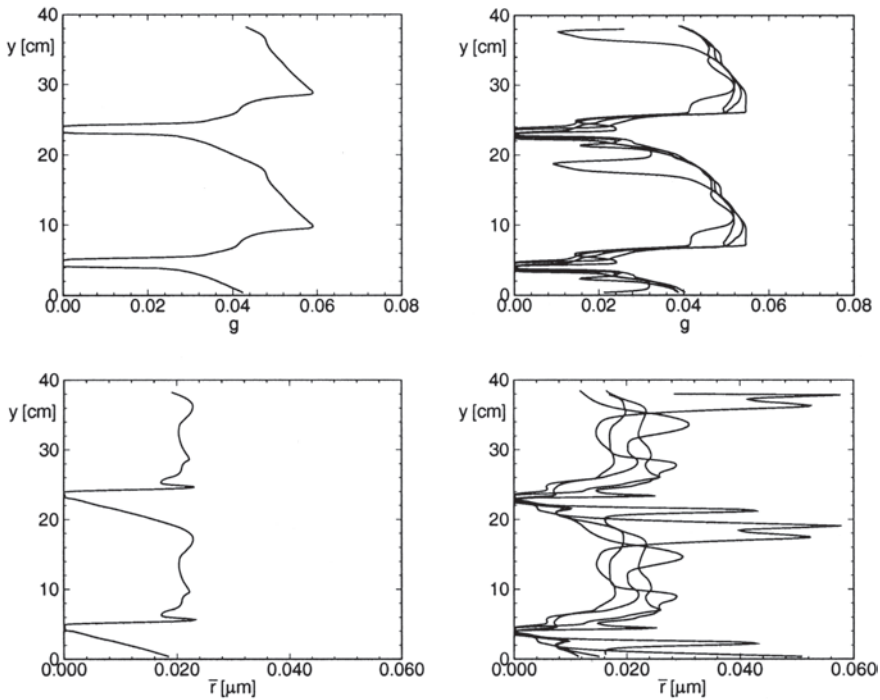
Fig. 52 Comparison of wetness and mean droplet size in control plane behind BAK-1 turbine cascade with and without rotor/stator interaction for (flow data, see Fig. 48)

compares pure homogeneous condensation of steam at the left-hand side with coupled homogeneous/heterogeneously condensing flow at right. Parameters for seeding with solid particles are the particle size

$r_{p,het} = 10^{-8}$ m and the number concentration $n_{het,0} = 10^{16}$ m^{-3}. Without seeding the flow through the stator remains adiabatic and the vapour experiences maximum supersaturation causing maximum
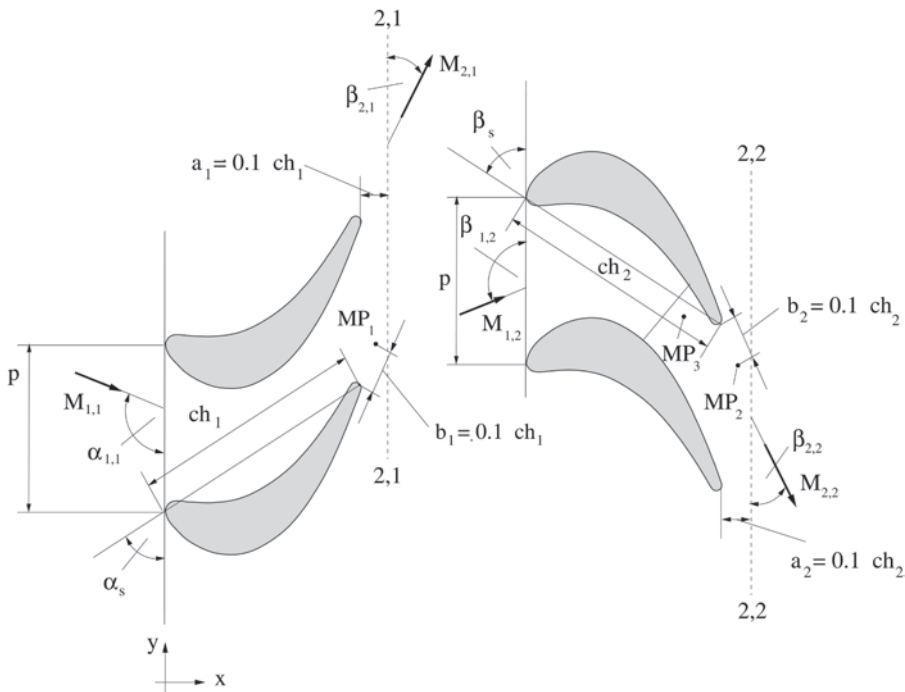
Fig. 53 Layout and data of VKI-1 turbine stage for simulation of rotor/stator interaction by means of sliding interface
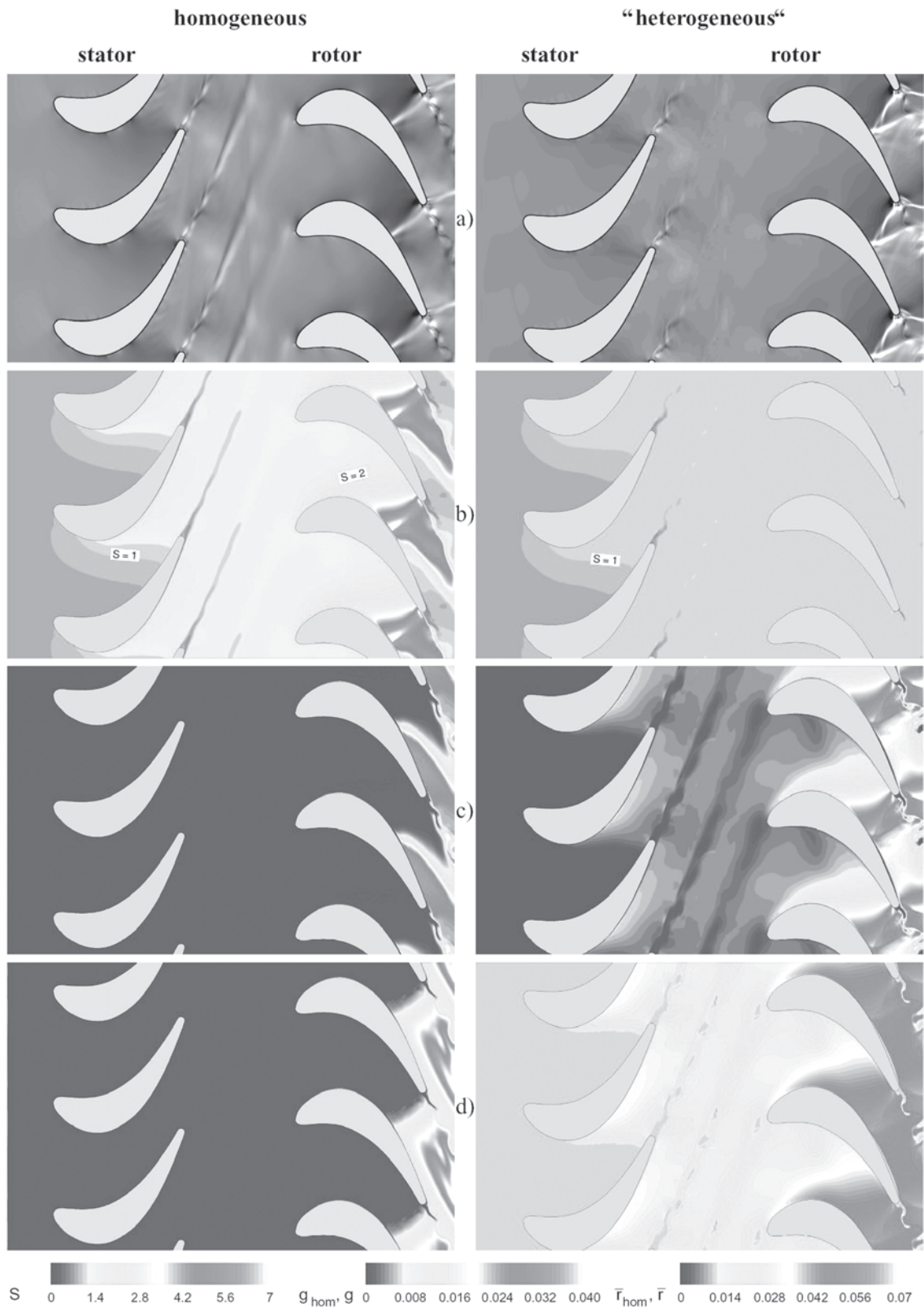
Fig. 54 Rotor/stator interaction in condensing steam flow through VKI-1 stage. Instantaneous pictures of homogeneously (left) and heterogeneously dominated (right) condensing turbulent flow; flow data: $T_{01} = 357.5$ K, $p_{01} = 0.417$ bar, $\beta_1 = 120°$, $p_2 = 0.194$ bar, $M_{2,is} = 1.13$, $Re_{2rotor} = 1.13 \times 10^6$, $n_{het,\,0} = 10^{16}$ m^{-3}, $r_{p,\,het} = 10^{-8}$ m. From top: Schlieren-type simulation, saturation ratio, $S = p_v(T)/p_{v,sat}(T)$, wetness g and mean droplet radii $\bar{r}$

non-equilibrium losses in the rotor. With seeding particles, the supersaturation of the vapour disappears more or less completely and $S \sim 1$ in the entire flow regime of the stage. The alteration of the dispersed structure of the liquid phase is quite obvious and significant. Droplet formation begins in the stator, the condensate passes through the interface and is convected into the rotor. Comparing the Schlieren simulations, it is recognized that the trailing edge shock system intensifies after seeding. In this special case, the increase of the related gas dynamic losses of the shocks over-compensates the reduction of thermodynamic non-equilibrium losses by seeding to some extent. The more intense shock system at the trailing edge also forces the shedding frequency to increase, from $f_{vs,rotor} = 16.2$ kHz in homogeneously condensing flow to 18.5 kHz with seeding. Simultaneously, the stator frequency decreases a bit from $f_{vs,rotor} = 11.6$ kHz in homogeneously condensing flow to 10.8 kHz with seeding. In single-phase flow, the reference data are $f_{vs,rotor} = 15.2$ kHz for the rotor and $f_{vs,stator} = 11.6$ kHz. So far, the previously observed trend in this cascade is confirmed, condensation tends to increase the shedding frequency from the rotor blades, independent of the nature of the phase transition as homogeneous or heterogeneous condensation. For more details, see Winkler and Schnerr [58] and Schnerr [59].

CONCLUSION

The subject considered here has two different aspects. The first concerns the dynamics of high-speed fluid mechanics with phase transition, respectively the stability of compressible fluids with energy supply. The second aspect concerns the impact of such instabilities on flows through large-scale steam turbines. For CFD techniques modelling of such flows requires many assumptions and simplifications, even in case of two-dimensional flows. Extension to three-dimensional flows through multi-stage machines with accurate resolution of all relevant time-scales of these instabilities increases the CPU by orders. However, we have seen that already most simple flow models make the main driving mechanism visible and understandable. In addition to the self-excitation and forced excitation, other mechanisms exist. For instance, if in transonic single-phase flow through an axial cascade buffeting establishes periodic separation, periodic choking, etc. and if this single-phase self-excited instability becomes superposed by the diabatic self-excited instability of the phase transition processes. Depending on the frequency of the two periodic systems non-linear interactions have to be expected with the formation of higher order bifurcations.

REFERENCES

1 **Zierep, J.** Similarity laws and modeling. In *Gasdynamics* (Ed. P. P. Wegener) 1971 (Marcel Dekker, New York).

2 **Zierep, J.** *Ähnlichkeitsgesetze und Modellregeln der Strömungslehre*, 3rd edition, 1991 (Wissenschaft & Technik, G. Braun-Verlag, Karlsruhe).

3 **Bartlmä, F.** *Gasdynamik der Verbrennung*, 1975, (Springer-Verlag, Wien-New York).

4 **Bartlmä, F.** Berechnung des Strömungsvorganges bei Überschreiten der kritischen Wärmezufuhr. DVL bericht 168, 1961.

5 **Delale, C. F., Schnerr, G. H.,** and **Zierep, J.** The mathematical theory of thermal choking in nozzle flows. *Z. Angew. Math. Phys.*, 1993, **44**, 943.

6 **Möhring, W.** On flows with heat addition in Laval nozzles. In *Recent developments in theoretical and experimental fluid mechanics* (Eds U. Müller, K. G. Roesner, and B. Schmidt) 1979, pp. 179–185 (Springer-Verlag, Berlin).

7 **Younis, S.** *Stationäre Strömungen durch Lavaldüsen mit Wärmezufuhr.* Diplomarbeit Fakultät für Maschinenbau, Universität Karlsruhe (TH), 1987.

8 **Bakhtar, F., Young, J. B., White, A. J.,** and **Simpson, D. A.** Classical nucleation theory and its application to condensing steam flow calculations. *Proc. IMechE, Part C: J. Mechanical Engineering Science*, 2005, **219**(C12), 1315–1333.

9 **Ford, I. J.** Statistical mechanics of water droplet nucleation. *Proc. Instn Mech. Engrs, Part C: J. Mechanical Engineering Science*, 2004, **218**(C8), 883–899.

10 **Volmer, M.** *Kinetik der Phasenbildung*, 1939 (Steinkopff-Verlag, Leipzig).

11 **Frenkel, J.** *Kinetic theory of liquids*, 1946 (Oxford University Press, New York) reprinted in 1955 by Dover, New York.

12 **Dillmann, A.** and **Meier, G. E. A.** A refined droplet approach to the problem of homogeneous nucleation from the vapor phase. *J. Chem. Phys.*, 1991, **94**(5), 3872–3884.

13 **Lamanna, G.** *On nucleation and droplet growth in condensing nozzle flows.* PhD Thesis, Technical University Eindhoven, The Netherlands, 2000.

14 **Mosnier, F. P.** *Unsteady supersonic flow with heat addition due to condensation.* PhD Thesis, Graduate School of the Yale University, New Haven, Connecticut, USA, 1976.

15 **Schmidt, B.** *Beobachtungen über das Verhalten der durch Wasserdampf-Kondensation ausgelösten Störungen in einer Überschall-Windkanaldüse.* Dissertation Fakultät für Maschinenbau, Universität Karlsruhe (TH), 1962.

16 **Barschdorff, D.** Kurzzeitfeuchtemessung und ihre Anwendung bei Kondensationserscheinungen in Laldüsen. *Strömungsmechanik und Strömungsmaschinen*, 1967, Vol. 6, pp. 18–39 (G. Braun-Verlag, Karlsruhe).

17 **Adam, S.** *Numerische und experimentelle Untersuchung instationärer Düsenströmungen mit Energiezufuhr durch homogene Kondensation.* Dissertation Fakultät für Maschinenbau, Universität Karlsruhe (TH), 1996.

18 **Saltanov, G. A.** and **Tkalenko, R. A.** Investigation of transonic unsteady-state flow in presence of phase

transformation. *Zh. Prikl. Mek. i Tek. Fiz. (UdSSR)*, 1975, **6**, 42–48.

19 **Bakhtar, F., White, A. J.,** and **Mashmoushy, H.** Theoretical treatments of two-dimensional two-phase flows of steam and comparison with cascade measurements. *Proc. IMechE, Part C: J. Mechanical Engineering Science*, 2005, **219**(C12), 1335–1355.

20 **Skillings, S. A.** and **Jackson, R.** A robust time-marching solver for one-dimensional nucleating steam flows. *Int. J. Heat and Fluid Flow*, 1987, **8**(2), 139–143.

21 **White, A. J.** and **Young, J. B.** A time marching method for the prediction of two-dimensional unsteady flows of condensing steam. *J. Propul. Power*, 1993, **9**, 579–587.

22 **Guha, A.** and **Young, J. B.** Time-marching prediction of unsteady condensation phenomena due to supercritical heat addition. IMechE C423/057, 1991, pp. 167–177.

23 **Mundinger, G.** *Numerische Simulation instationärer Lavaldüsenströmungen mit Energiezufuhr durch homogene Kondensation.* Dissertation Fakultät für Maschinenbau, Universität Karlsruhe (TH), 1994.

24 **Young, J. B.** The fundamental equations of gas-droplet multiphase flow. *Int. J. Multiphase Flow*, 1995, **21**, 175–191.

25 **Schnerr, G. H.** and **Dohrmann, U.** Drag and lift in non-adiabatic transonic flow. *AIAA J.*, 1994, **32**(1), 101–107.

26 **Adam, S.** and **Schnerr, G. H.** Instabilities and bifurcation of non-equilibrium two-phase flows. *J. Fluid Mech.*, 1997, **348**, 1–28.

27 **Matsuo, K., Kawagoe, S., Sonoda, K.,** and **Setoguchi, T.** Oscillations of Laval nozzle flow with condensation – Part 2. *Bull. JSME*, 1985, **28**, 88–93.

28 **Schnerr, G. H., Adam, S.,** and **Mundinger, G.** New modes of periodic shock formation in compressible two-phase flows. In Proceedings of IUTAM Symposium *Waves in gas/liquid and liquid/vapor two-phase systems* (Eds S. Morioka and L. van Wijngaarden), 1994, pp. 377–386 (Kluwer Academic Publishers: Dordrecht, Boston, London).

29 **Deych, M. E., Filippov, G. A., Saltanov, G. A., Kurshakov, A. V., Kukushkin, A. N.,** and **Nozdrin, G. N.** Experimental study of unsteady phenomena in a flow of condensing vapor in nozzles. *Fluid Mech. – Soviet Res.*, 1974, **3**, 151–157.

30 **Barschdorff, D.** Verlauf der Zustandsgrößen und gasdynamische Zusammenhänge der spontanen Kondensation reinen Wasserdampfes in Lavaldüsen. *Forschung im Ingenieurwesen*, 1971, **37**(5), 146–157.

31 **Collignan, B.** *Contribution à l'étude de la condensation instationnaire en ecoulement transsonique.* PhD Thesis, Université Pierre & Marie Curie, Paris, France, 1994.

32 **Zierep, J.** and **Lin, S.** Ein Ähnlichkeitsgesetz für instationäre Kondensationserscheinungen in der Lavaldüse. *Forschung im Ingenieurwesen*, 1968, **34**, 97–99.

33 **Wegener, P. P.** and **Cagliostro, D. J.** Periodic nozzle flow with heat addition. *Combust. Sci. Technol.*, 1973, **6**, 269–277.

34 **Wegener, P. P.** and **Mosnier, F. P.** Periodic transonic flow with heat addition: new results. *Combust. Sci. Technol.*, 1981, **24**, 179–189.

35 **Sichel, M.** *Unsteady transonic flow with heat addition.* PhD Thesis, Department of Aerospace Engineering, The University of Michigan, Ann Arbor, Michigan, USA, 1976.

36 **Sichel, M.** Unsteady transonic nozzle flow with heat addition. *AIAA J.*, 1981, **19**, 165–171.

37 **Petr, V.** Stability of transonic two-phase flow with terminating shock wave. In Proceedings of Second ISAIF International Symposium on *Experimental and computational aerothermodynamics*, Prague, 12–15 July 1993, pp. 441–448.

38 **Delale, C. F., Lamanna, G.,** and **van Dongen, M. E. H.** On the stability of stationary shock waves in nozzle flows with homogeneous condensation. *Phys. Fluids*, 2001, **13**(9), 2706–2720.

39 **Schnerr, G. H.** 2-D transonic flow with energy supply by homogeneous condensation: onset condition and 2-D structure of steady Laval nozzle flow. *Exp. Fluids*, 1989, **7**, 145–156.

40 **Delale, C. F.** and **Crighton, D. G.** Prandtl–Meyer flows with homogeneous condensation. Part 1 subcritical flows. *J. Fluid Mech.*, 1998, **359**, 23–47.

41 **Delale, C. F.** and **Crighton, D. G.** Prandtl–Meyer flows with homogeneous condensation. Part 2 supercritical flows. *J. Fluid Mech.*, 2001, **430**, 231–265.

42 **Smith, L. T.** Experimental investigation of the expansion of moist air around a sharp corner. *AIAA J.*, 1971, **9**, 2035–2037.

43 **Frank, W.** *Stationäre und instationäre Kondensationsvorgänge bei einer Prandtl–Meyer-Expansion.* Habilitationsschrift Fakultät für Maschinenbau, Universität Karlsruhe (TH), 1979.

44 **Simpson, D. A.** and **White, A. J.** Viscous and unsteady flow calculations of condensing steam in nozzles. *Int. J. Heat Fluid Flow*, 2005, **26**(1), 71–79.

45 **Heiler, M.** *Instationäre Phänomene in homogen/heterogen kondensierenden Düsen- und Turbinenströmungen.* Dissertation Fakultät für Maschinenbau, Universität Karlsruhe (TH), 1999.

46 **Goodheart, K. A.** *3-D Transonic flow dynamics with non-equilibrium condensation.* Dissertation Fakultät für Maschinenwesen, Technische Universität München, 2004.

47 **Gyarmathy, G.** and **Spengler, P.** *Flow fluctuations in multistage thermal turbomachinery*, 1974, pp. 95–141 (Traupel-Festschrift, Juris-Verlag, Zürich).

48 **Whirlow, D. K., Closkey, T. J., Davis, J., Chen, S., Kadambi, J. R.,** and **Farn, C. L. S.** Flow instabilities in low pressure steam turbine blade passages. ASME paper 84-JPGC-GT-14, 1984.

49 **Denton, J. D.** and **Xu, L.** The trailing edge loss of transonic turbine blades. *J. Turbomach.* 1990, **112**, 277–285.

50 **Guha, A.** and **Young, J. B.** The effect of flow unsteadiness on the homogeneous nucleation of water droplets in steam turbines. *Philos. Trans. R. Soc. Lond. A*, 1994, **349**, 445–472.

51 **Cicatelli, C.** and **Sieverding, C. H.** The effect of vortex shedding on the unsteady pressure distribution around the trailing edge of a turbine blade. *J. Turbomach.*, 1997, **119**, 810–819.

52 **Bream, S., Laali, A. R., Dorey, J. M.,** and **Kleitz, A.** Modelling of unsteady condensing steam

C09205 © IMechE 2005

Proc. IMechE Vol. 219 Part C: J. Mechanical Engineering Science

flow: two-dimensional approach using exact thermo-dynamic formulations. In Proceedings of European Conference on *Turbomachinery, fluid dynamics and thermodynamics*, Antwerp, 5–8 March 1997.

53 **Bakhtar, F.** and **Heaton, A. V.** An examination of the effect of wake chopping on droplet sizes in steam turbines. In Proceedings of BNES Conference Technology on *Turbine plant operating with wet steam*, London, October 1988.

54 **Bakhtar, F., Ebrahimi, M.,** and **Bamkole, B. O.** On the performance of a cascade of turbine rotor tip section blading in nucleating steam – Part I: surface pressure distribution. *Proc. Instn Mech. Engrs, Part C: J. Mechanical Engineering Science*, 1995, **209**(C2), 115–124.

55 **Hodson, H. P.** An inviscid blade-to-blade prediction of wake-generated unsteady flow. *J. Eng. Gas Turb. Power*, 1985, **107**, 337–343.

56 **Hodson, H. P.** Measurements of wake-generated unsteadiness in the rotor passages of axial flow turbines. *J. Eng. Gas Turb. Power*, 1985, **107**, 467–476.

57 **Winkler, G.** *Laufrad-Leitrad-Wechselwirkung in homogen–heterogen kondensierenden Turbinenströmungen*. Dissertation Fakultät für Maschinenbau, Universität Karlsruhe (TH), 2000.

58 **Winkler, G.** and **Schnerr, G. H.** Nucleating unsteady flows in low pressure steam turbien stages. In Proceedings of 4th European Conference on *Turbomachinery, fluid dynamics and thermodynamics* (Eds G. Bois, R. Decuypere, and F. Martelli), France, Italy, 20–23 March 2001, pp. 793–802 (SGEditoriali, Padova).

59 **Schnerr, G. H.** Unsteady nonadiabatic transonic two-phase flow. In Proceedings of IUTAM Symposium *Transsonicum IV* (Ed. H. Sobieczky), 2003, pp. 369–380 (Kluwer Academic Publishers, Dordrecht, Boston, London).

APPENDIX

Notation

A	cross-sectional area of one-dimensional flow model (m^2)
c	speed of sound (m/s), blade chord length (m)
c_v	specific heat at constant volume (J/(kg/K))
c_p	specific heat at constant pressure (J/(kg/K))
f	frequency (s^{-1}), arc length of blade ($-$)
g	wetness ($-$), condensate mass ($kg_{condesate}/kg_{mixture}$)
h	specific enthalpy (J/kg)
J	homogeneous nucleation rate ($m^{-3}\,s^{-1}$)
m	dimensionless mass addition ($-$)
M	Mach number ($-$)
p	static pressure (bar), pitch (m)
q	specific amount of heat addition (J/kg)
Q	dimensionless amount of heat addition ($-$)
r	droplet radius (m)

R	nozzle throat radius, (m), specific gas constant (J/(kg K))
Re	Reynolds number ($-$)
s	specific entropy (J/(kg K))
S	saturation ratio ($-$)
St	Strouhal number ($-$)
t	time (s)
T	absolute temperature (K), time of one oscillation period (s)
w	flow velocity of one-dimensional flow model (m/s)
x	Cartesian coordinate (m), mixing ratio ($g_{vapor}/kg_{dry\ air}$)
y	Cartesian coordinate, half of the throat height of two-dimensional plane nozzle (m)

β	flow angle of axial cascade ($°$)
γ	specific heat ratio ($-$)
Δ	difference ($-$)
ε	specific amount of mass addition ($kg/(m^2\,s)$)
ρ	density (kg/m^3)
ϕ	relative humidity (per cent)

Superscripts

$*$	critical state at $M=1$ and at sonic throat
$'$	small disturbance
$-$	mean value

Subscripts

e	nozzle exit plane
f	frozen
het	properties related to heterogeneous condensation
max	maximum value
p	particle
s	saturation value
vs	vortex shedding
rotor	flow property in rotor
stator	flow property in stator
0	reservoir, stagnation value
1	state ahead of heat addition, ahead of shock, at control plane ahead of axial cascade
2	state behind of heat addition, behind shock, at control plane behind axial cascade

C09205 © IMechE 2005